Agenzia nazionale per le nuove tecnologie,
l'energia e lo sviluppo economico sostenibile

MINISTERO DELLO SVILUPPO ECONOMICO

Ricerca di Sistema elettrico

Schemi Numerici e Condizioni al Contorno Non Riflessive per la Simulazione di Gas Reali

E. Giacomazzi, D. Cecere, N. Arcidiacono, F.R. Picchia

Report RdS/PAR2016/183

SCHEMI NUMERICI E CONDIZIONI AL CONTORNO NON RIFLESSIVE PER LA SIMULAZIONE DI GAS REALI

E. Giacomazzi, D. Cecere, N. Arcidiacono, F.R. Picchia (ENEA)

Settembre 2017

Report Ricerca di Sistema Elettrico
Accordo di Programma Ministero dello Sviluppo Economico - ENEA
Piano Annuale di Realizzazione 2016
Area: Generazione di energia con basse emissioni di carbonio
Progetto: Polo Tecnologico del SULCIS: Tecnologie e Metodologie "Low Carbon" e Edifici a Energia Quasi Zero (nZEB)
Obiettivo: Parte A - a.2 - Cicli a CO2 supercritica
Task a.2.3 - Studi mediante simulazione numerica (HeaRT)
di processi di ossi-combustione in atmosfera di CO2 supercritica
Responsabile del Progetto: Franca Rita Picchia, ENEA

Indice

Sommario

La crescente tendenza verso un uso piú sostenibile dei combustibili fossili per la generazione di potenza ha aperto nuovi orizzonti applicativi per i cicli a CO_2 supercritica ($S-CO_2$), che hanno le potenzialitá per rappresentare una risposta efficace ad alcuni temi di grande attualitá: la flessibilitá operativa dei sistemi di generazione da fonte fossile a supporto della generazione da fonte rinnovabile non programmabile, e la riduzione delle emissioni inquinanti e climalteranti. L'estrema compattezza dei cicli a $S-CO_2$ puó rappresentare una soluzione mirata alla ricerca di flessibilitá operativa; inoltre, é ben accoppiata sia con l'efficienza termodinamica sia con la potenziale applicazione delle tecnologie di cattura e stoccaggio della CO_2. Gli studi effettuati nelle precedenti annualitá hanno evidenziato un significativo allineamento tra le esigenze di un sistema elettrico de-carbonizzato ad alta penetrazione di rinnovabili non programmabili e le potenzialitá in termini di flessibilitá, risposta dinamica, efficienza, emissioni e performance economica che i cicli a $S-CO_2$ alimentati con ossi-combustione di gas naturale possono potenzialmente esporre.

Nella precedente annualitá, il codice HeaRT sviluppato da ENEA é stato testato con simulazioni numeriche di problemi con la simultanea presenza di fasi liquide e gassose. In particolare, é stato identificato un caso test relativo al mescolamento turbolento a 40 bar tra un getto di azoto liquido iniettato a 118 K e 5 m/s con un getto coassiale di idrogeno gassoso a 270 K e 120 m/s. Le simulazioni hanno evidenziato una insufficiente robustezza degli schemi numerici implementati in HeaRT in presenza di forti gradienti spaziali di densitá, soprattutto dovuti a "discontinuitá materiali o di contatto": queste discontinuitá sono quelle che si incontrano quando due fluidi con proprietá diverse (in particolare, velocitá del suono e calori specifici, in base alla nostra esperienza) sono a contatto. E' quindi nata la necessitá di identificare, valutare ed implementare uno schema numerico di integrazione spaziale piú robusto.

Nella presente annualitá é stata inizialmente fatta una ricerca approfondita sugli schemi numerici di integrazione spaziale giá presenti in letteratura, adatti a simulare (senza oscillazioni numeriche spurie) flussi in condizioni di gas reale con presenza di un'interfaccia liquido/gas. La nascita di oscillazioni nell'intorno di discontinuitá di contatto con l'uso del codice HeaRT é fondamentalmente dovuta alla formulazione pienamente conservativa delle equazioni di trasporto implementate. Sono state identificate due possibili strategie per evitare il problema:

1. implementare un'equazione di trasporto per la pressione al posto di quella per l'energia totale, ed utilizzare la tecnica LAD (Local Artificial Dissipation), cioé aggiungere termini di viscositá artificiale alle equazioni di trasporto per evitare o smorzare oscillazioni numeriche spurie;

2. implementare lo schema numerico $AUSM^+-up$ che, sulla base della letteratura esistente, sembra avere particolari capacitá di robustezza.

La prima strategia é stata studiata a livello teorico in modo approfondito, e la tecnica LAD é stata implementata nel codice HeaRT. La seconda strategia é stata pure studiata in modo dettagliato sulla base della letteratura esistente, quindi implementata e testata diffusamente. L'aver ottenuto degli ottimi risultati con lo schema $AUSM^+-up$, unito alla sua semplicitá ed al fatto che l'adozione di un'equazione di trasporto per la pressione comporterebbe la perdita della proprietá di conservativitá delle equazioni, ha portato alla scelta della seconda strategia come soluzione ai problemi riscontrati nella precedente annualitá. Si osserva che nel codice HeaRT lo schema $AUSM^+-up$ é stato accoppiato ad una procedura di interpolazione WENO (5-3 ordine) per la ricostruzione degli stati destro e sinistro delle variabili di campo, con l'ulteriore possibilitá di ricorrere ad una interpolazione meno costosa, ma anche meno accurata, quella QUICK (3 ordine).

In particolare, lo schema $AUSM^+-up$ ha superato con successo i seguenti test:

1. problema mono-dimensionale di SOD (shock-tube, con salto iniziale di pressione 150 bar - 15 bar, rispettivamente a sinistra e a destra di un setto), con presenza di un'espansione, una discontinuitá di contatto ed un urto, in condizioni di gas reale (vedi Fig. 0.1);

2. problema mono-dimensionale di una discontinuitá materiale ferma ed in movimento;

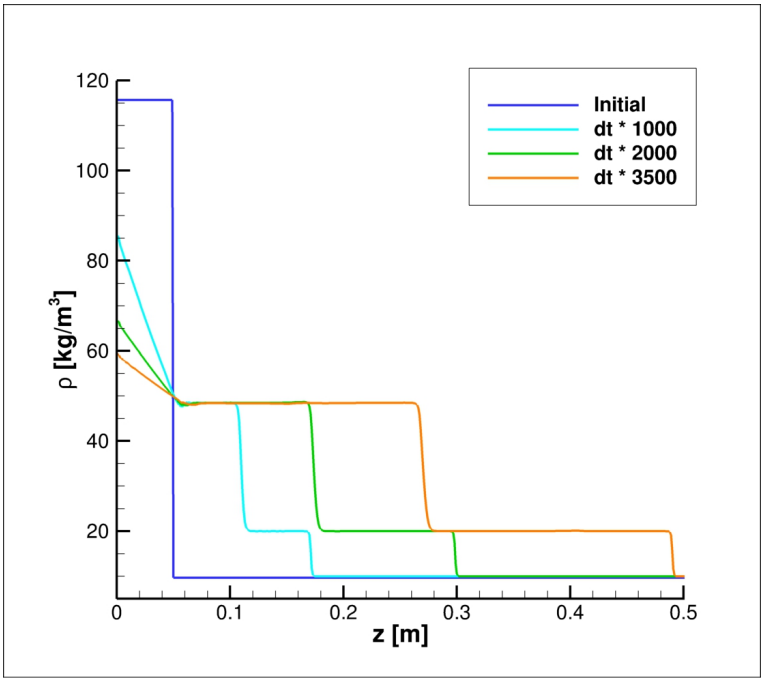

Figura 0.1: Soluzione del campo di densit, a diversi istanti, del problema mono-dimensionale di SOD con gas reale: il campo é inizializzato con 150 bar e 15 bar, rispettivamente a sinistra e a destra di un setto posto a 0.05 m.

3. shear-layer temporale, bidimensionale, tra un getto centrale di metano ed uno coassiale di ossigeno, entrambi gassosi ed a 300 K, in condizioni di gas ideale ad 1.5 bar;

4. shear-layer temporale (ingresso/uscita periodici), bidimensionale, tra un getto centrale di azoto liquido (118 K, 5 m/s) ed uno coassiale di idrogeno gassoso (270 K, 120 m/s), in condizioni di gas reale a 40 bar.

Si sottolinea che il quarto test é stato derivato da quello utilizzato nella precedente annualitá e che aveva evidenziato i problemi numerici: la semplificazione del test ad uno shear-layer temporale ha permesso di eseguire simulazioni di lunga durata (un milione di passi temporali) per avere certezza della stabilitá del calcolo. La Fig. 0.2 mostra per un certo istante, le distribuzioni di temperatura e di densitá. Si nota che in alcune zone di mescolamento tra i due getti, la temperatura scende (circa 107 K) al di sotto di quella dell'azoto liquido: questo non é dovuto ad oscillazioni numeriche spurie bensí é un effetto di gas reale dovuto al fatto che la curva della temperatura di mescolamento adiabatica tra azoto ed idrogeno a 40 bar passa per la zona di equilibrio bifase. Infine, é stata affrontata la simulazione di uno shear-layer spaziale (ingresso/uscita effettivi), reagente, bidimensionale, di un getto centrale di metano a 100 m/s ed uno coassiale di ossigeno a 25 m/s, entrambi gassosi a 300 K ed in condizioni di gas reale a 150 bar. Tale condizione é tipica degli ossi-combustori dei cicli a $S - CO_2$. Si osserva che le condizioni non-riflessive di uscita sono state estese per lavorare con gas reali: questo é stato pure oggetto di implementazione e test nella presente annualitá. La Fig. 0.3 mostra le distribuzioni istantanee di temperatura e fattore di comprimibilitá per questo caso. Si osserva come la temperatura massima superi i 3000 K della temperatura adiabatica attesa, a causa del meccanismo cinetico semplificato adottato (mancanza di reazioni endotermiche delle principali specie radicali). Il fronte appare notevolmente corrugato, evidenziando la presenza di piccole scale. Il fattore di comprimibilitá evidenzia invece la tendenza al comportamento di gas ideale nella regione occupata dai gas combusti, e ad un comportamento di gas reale altrove, con forti gradienti spaziali.

In conclusione, con le notevoli migliorie apportate agli schemi numerici ed alle condizioni al contorno non-riflessive, il codice HeaRT sviluppato da ENEA é ora uno strumento di calcolo numerico parallelo avanzato, adeguato per la simulazione fluidodinamica di flussi turbolenti, reagenti e non, in condizioni di gas reale. A titolo di esempio é stata infine condotta una simulazione introduttiva alle problematiche che verranno affrontate

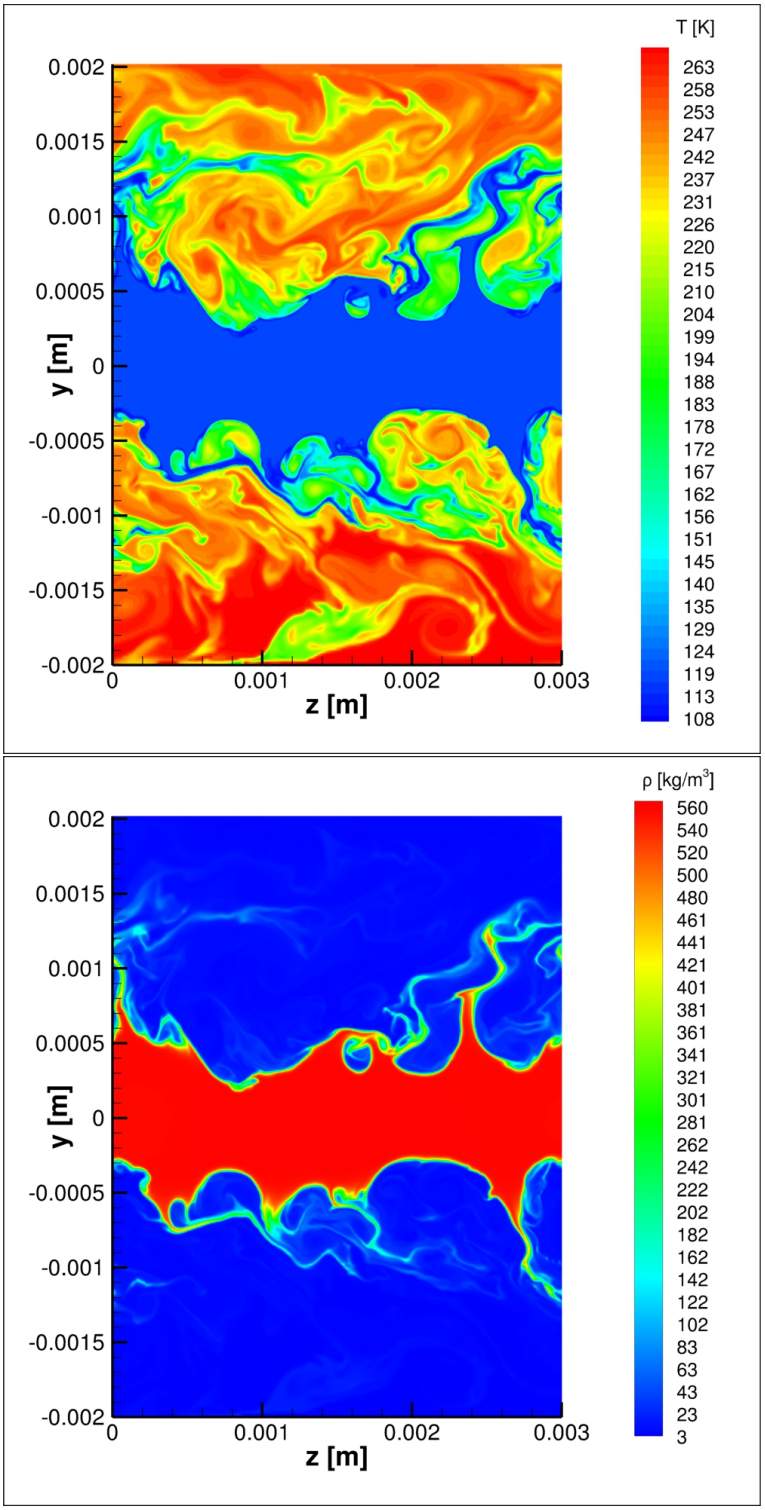

Figura 0.2: Distribuzioni istantanee di temperatura e densitá per lo shear-layer temporale azoto liquido / idrogeno gassoso a 40 bar in condizioni di gas reale.

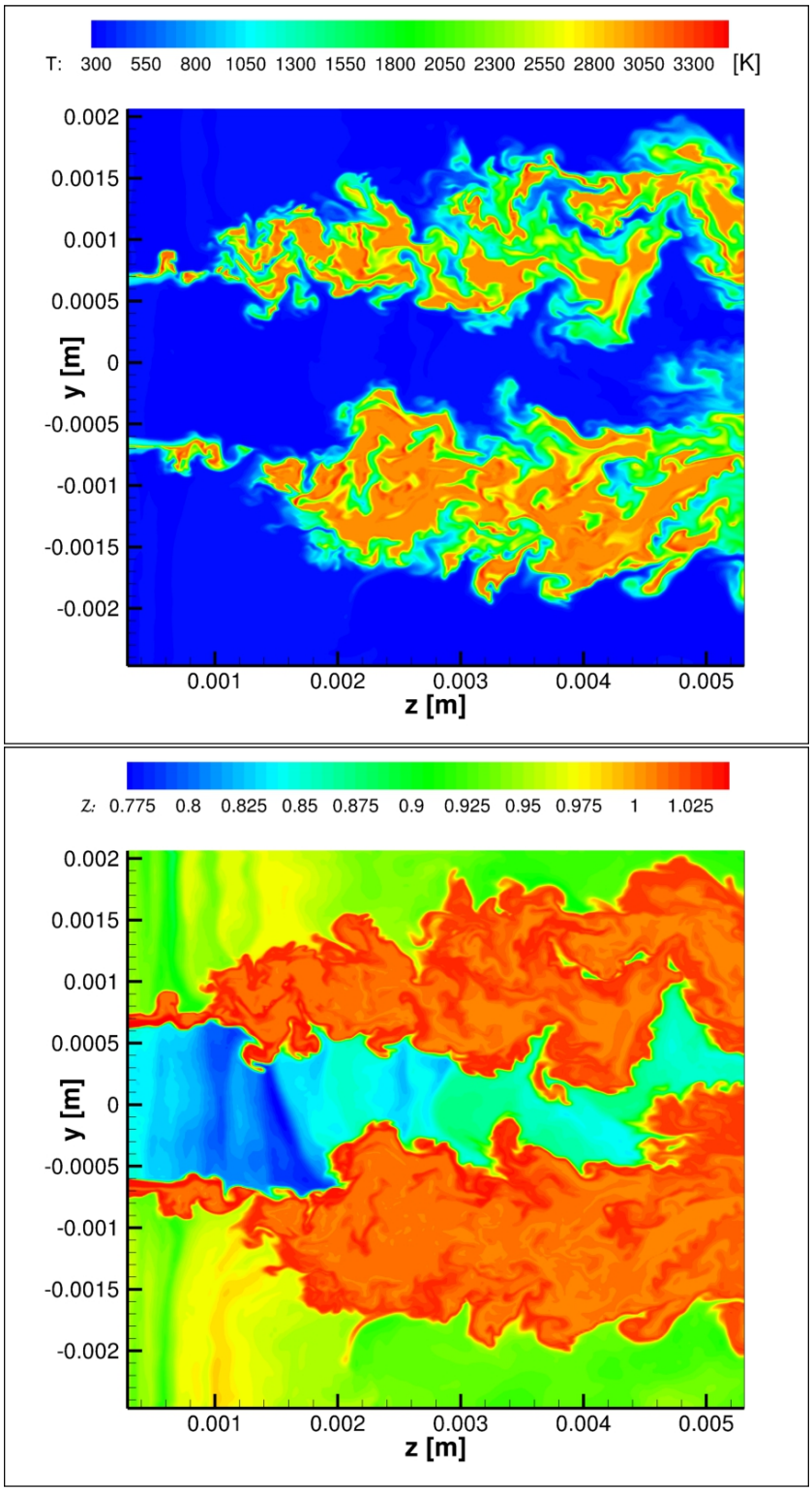

Figura 0.3: Distribuzioni istantanee di temperatura e fattore di comprimibilitá per lo shear-layer spaziale reagente metano / ossigeno gassosi a 150 bar in condizioni di gas reale.

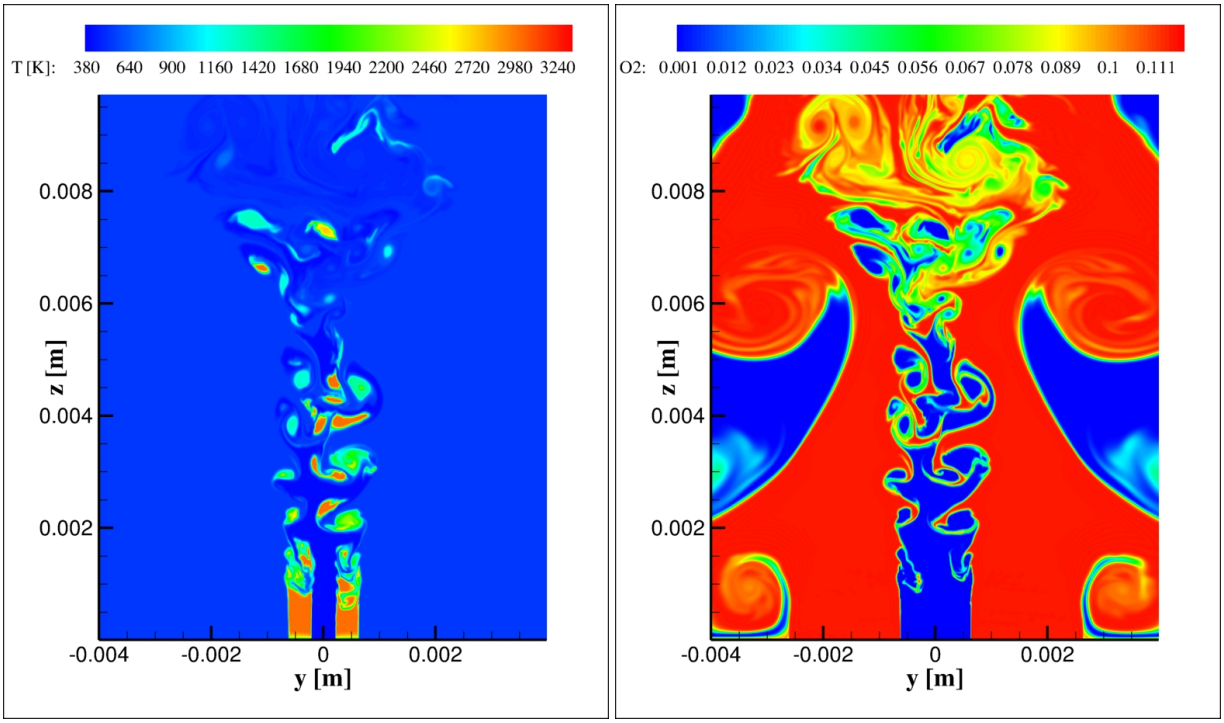

Figura 0.4: Distribuzioni istantanee di temperatura e frazione massica di ossigeno per il test esplorativo reagente metano / ossigeno (fortemente diluito in CO_2) gassosi a 295 bar in condizioni di gas reale.

nella prossima annualitá. Si tratta di un caso di combustione a 295 bar di un getto centrale di metano con uno coassiale di ossigeno, fortemente diluito in CO_2 (circa 88% in massa), iniettati in un'ulteriore corrente principale di CO_2. Tale simulazione, con puro scopo esplorativo, ha evidenziato notevoli problemi di ancoraggio della fiamma dovuti alla grande concentrazione di CO_2, ed una combustione poco efficiente, caratterizzata da pacchetti reagenti (con temperature che possono essere anche molto elevate) estremamente pericolosi per una eventuale turbina a valle del combustore (vedi Fig. 0.4). Questi temi saranno investigati con il codice HeaRT nelle prossime annualitá al fine di definire una opportuna strategia di combustione e le modalitá di iniezione dei reagenti, per arrivare al "concept-design" della piastra di iniezione di $CH_4/O_2/S - CO_2$ e del combustore di un ciclo a CO_2 supercritica con ossi-combustione.

1 Non-Reflecting Boundary Conditions for Real Gas Flows

In the LES context of compressible flows, it is highly recommended to use non-reflecting or partially reflecting boundary conditions to avoid spurious reflections of acoustic and entropic waves at boundaries. Such boundary conditions consist in solving the Navier-Stokes equations written in terms of waves (NSCBC method, Navier-Stokes Characteristic Boundary Conditions); depending on their propagation velocity, the waves moving towards the boundaries (outgoing waves) can be calculated from the computational field, while the waves moving from the boundaries (incoming waves) have to be modelled. The method is also useful to provide soft (or so called numerical) boundary conditions to the set of partial differential equations to be solved: the conservation equations are used at the boundary to complement the set of physical boundary conditions.

Although the approach goes back to the '80s, being developed by Rudy and Strikverda [1, 2] first, and then furtherly developed by Thomson [3, 4], nowadays, the reference paper for the non-reflecting or partially reflecting boundary conditions is that of Poinsot and Lele [5], later extended to reacting flows with variable transport molecular properties [6]. The NSCBC method consists in assuming Euler conditions (the inviscid conditions) and supplying additional relations (the viscous conditions) which refer to viscous or diffusion effects. The wave amplitude variations in the viscous multidimensional case is inferred by examining a local associated one-dimensional inviscid (LODI) problem: the transverse and viscous terms in the conservation equations written at the boundaries are neglected. Lodato [7] extended the NSCBC-1D approach for ideal gases to the three-dimensional case (NSCBC-3D) by adding transverse fluxes in wave computation.

1.1 Non-Reflecting Boundary Conditions for Real Gas Flows

Here is the formulation adopted for recasting the Navier-Stokes equations in terms of amplitude variation of the waves L_i incoming and outcoming from a boundary. It is observed that the approach adopted is the one extended to treat reacting flows in [6], but written using the formalism adopted in [5]. The approach pursued by Okong'o and Bellan [8] to extend the NSCBC-1D approach to real gases is also adopted here.

Considering a boundary orthogonal to the z direction, the equations are (in cylindrical coordinates; the cartesian formulation is obtained by replacing $r = 1$ and erasing the two source terms in the radial and azimuthal momentum equations):

- Continuity equation

$$r\frac{\partial \rho}{\partial t} + r d_1 + \frac{\partial r\rho U_r}{\partial r} + \frac{\partial \rho U_\vartheta}{\partial \vartheta} = 0 \tag{1.1}$$

- Momentum equations

$$r\frac{\partial \rho U_r}{\partial t} + r U_r d_1 + r\rho d_4 + \frac{\partial r\rho U_r^2}{\partial r} + \frac{\partial \rho U_r U_\vartheta}{\partial \vartheta} - \rho U_\vartheta^2 = -r\frac{\partial p}{\partial r} + \frac{\partial r\tau_{rr}}{\partial r} + r\frac{\partial \tau_{rz}}{\partial z} + \frac{\partial \tau_{r\vartheta}}{\partial \vartheta} - \tau_{\vartheta\vartheta} \tag{1.2}$$

$$r\frac{\partial \rho U_z}{\partial t} + r U_z d_1 + r\rho d_3 + \frac{\partial r\rho U_z U_r}{\partial r} + \frac{\partial \rho U_z U_\vartheta}{\partial \vartheta} = -r\frac{\partial p}{\partial z} + \frac{\partial r\tau_{zr}}{\partial r} + r\frac{\partial \tau_{zz}}{\partial z} + \frac{\partial \tau_{z\vartheta}}{\partial \vartheta} \tag{1.3}$$

$$r\frac{\partial \rho U_\vartheta}{\partial t} + r U_\vartheta d_1 + r\rho d_5 + \frac{\partial r\rho U_\vartheta U_r}{\partial r} + \frac{\partial \rho U_\vartheta^2}{\partial \vartheta} + \rho U_r U_\vartheta = -\frac{\partial p}{\partial \vartheta} + \frac{1}{r}\frac{\partial r^2\tau_{\vartheta r}}{\partial r} + r\frac{\partial \tau_{\vartheta z}}{\partial z} + \frac{\partial \tau_{\vartheta\vartheta}}{\partial \vartheta} \tag{1.4}$$

- Energy equation

$$\begin{aligned}&\frac{\partial \rho U}{\partial t}+\left(K+\sum_{i=1}^{N_s} Y_i H_i\right) d_1+\rho u_z d_3+\rho u_r d_4+\rho u_\vartheta d_5+\\&\rho \sum_{i=1}^{N_s} H_i L_{s,i}-\rho c_p L_6-R g_2 \frac{L_2}{\gamma-1}+\frac{1}{r} \frac{\partial \rho u_r U r}{\partial r}+\\&\frac{1}{r} \frac{\partial \rho u_\theta U}{\partial \theta}=-\frac{1}{r} \frac{\partial p u_r r}{\partial r}-\frac{1}{r} \frac{\partial p u_\theta}{\partial \theta}+\nabla \cdot[\tau u]-\\&\nabla \cdot q+\rho \sum_{i=1}^{N_s} Y_i f_i \cdot\left(u+V_i\right)\end{aligned} \tag{1.5}$$

- Mass fraction equations

$$\begin{aligned}&r \frac{\partial \rho Y_i}{\partial t}+r Y_i d_1+r \rho U_z \frac{\partial Y_i}{\partial z}+\frac{\partial r \rho U_r Y_i}{\partial r}+\frac{\partial \rho U_\vartheta Y_i}{\partial \vartheta}=-\frac{\partial r q_r^M}{\partial r}-\\&r \frac{\partial q_z^M}{\partial z}-\frac{\partial q_\vartheta^M}{\partial \vartheta}+r \dot{\omega}_i\end{aligned} \tag{1.6}$$

where

$$\begin{aligned}d_1 &= \frac{1}{a^2}\left(L_2+\frac{L_1+L_5}{2}\right)\\ d_2 &= \frac{L_1+L_5}{2}\\ d_3 &= \frac{L_5-L_1}{2 \rho a}\\ d_4 &= L_3\\ d_5 &= L_4\\ d_6 &= L_6\end{aligned} \tag{1.7}$$

$$\begin{aligned}L_1 &= \left(U_z-a\right)\left(\frac{\partial p}{\partial z}-\rho a \frac{\partial U_z}{\partial z}\right)\\ L_2 &= U_z\left(a^2 \frac{\partial \rho}{\partial z}-\frac{\partial p}{\partial z}\right)\\ L_3 &= U_z \frac{\partial U_r}{\partial z}\\ L_4 &= U_z \frac{\partial U_\vartheta}{\partial z}\\ L_5 &= \left(U_z+a\right)\left(\frac{\partial p}{\partial z}+\rho a \frac{\partial U_z}{\partial z}\right)\\ L_{s,i} &= U_z \frac{\partial Y_i}{\partial z}\\ L_6 &= \sum_{i=1}^{N_s} \frac{W}{W_i} T L_{s,i} R g_{1_i}\end{aligned} \tag{1.8}$$

and

$$Rg_{1_i} = \frac{\rho v_i}{\alpha_v W T} \tag{1.9}$$

$$Rg_2 = \alpha_v T \tag{1.10}$$

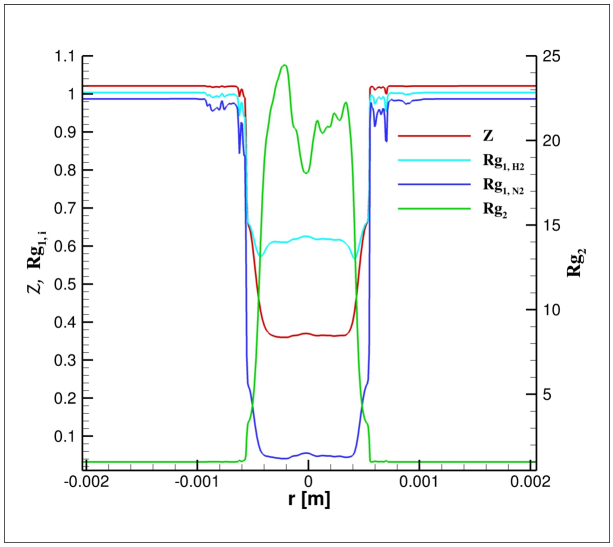

Figura 1.1: Plot of the distribution of the compressibility factor $\mathcal{Z}$ and the real gas corrections for an instantaneous flowfield of the non-reacting shear-layer considered in Section 1.3.

The terms $Rg1_i$ and Rg_2 in (1.5) have been derived by comparing the formalism and formulation introduced by Okong'o and Bellan [8] to extend the NSCBC-1D approach to real gases with the commonly used ideal gas formulation [5, 6]; the coefficient α_v is the expansivity coefficient and can be evaluated by means of

$$\alpha_v = \frac{1}{v}\left(\frac{\partial v}{\partial T}\right)_{p.Y_\alpha} = -\frac{\left(\frac{\partial p}{\partial T}\right)_{v,Y_\alpha}}{v\left(\frac{\partial p}{\partial v}\right)_{T,Y_\alpha}} \tag{1.11}$$

while the partial molar volume v_α is

$$v_\alpha = \left(\frac{\partial v}{\partial X_\alpha}\right)_{p,T,Y_\beta,\beta\neq\alpha} = \left(\frac{\partial \mu_\alpha}{\partial p}\right)_{T,X_\alpha,X_\beta} \tag{1.12}$$

It is observed that the corrections become equal to one when the gas becomes ideal, i.e., the compressibility factor is one: this is shown in Fig. 1.1 related to the exit of an instantaneous flowfield of the non-reacting shear-layer considered in Section 1.3.

In the following we briefly report the waves that have to be modelled at outflow and inflow boundaries to avoid or at least reduce spurious reflections.

1.2 Outflow and Inflow

In case of a supersonic outflow, there are no incoming waves: the complete set of (outgoing) waves can be computed from the inner flowfield. In case of a subsonic outflow, there is just one incoming wave that has to be modelled. Its amplitude has to be nil, i.e., $L_1 = 0$, to avoid reflections. However, this strategy is useful if the total time to be simulated is sufficiently short not to experience a dramatic pressure drift. In fact, when imposing $L_1 = 0$ the nominal pressure is not specified at boundaries; it is in the simulation just as an initial condition. As a matter of fact, the pressure will drift during the computation towards lower values. When compressibility effects are not important and when the actual value of pressure does not affect any physical mechanism, the flowfield obtained will be fine since the pressure spatial gradient is the driving force in the momentum equation. However, going on with the simulation, some floating point exception will be inevitably encountered in the routines dealing with molecular property calculation.

Hence, the importance of outflow partially reflecting boundary conditions to keep the operating pressure around a specified value, thus avoiding its drifting in long time computations. To fulfill this, for an outflow

boundary located on the right side of the computational domain (the flow comes from the left side) the incoming wave amplitude is modelled as

$$L_1 = \sigma \frac{\left(1 - M^2\right) c}{L_z} \left(p - p_\infty\right) - \frac{1}{2}\dot{Q}, \tag{1.13}$$

where σ is a constant (its theoretical optimal value is 0.27) to control the level of reflection and the time response of the boundary itself to perturbations, L_z is the acoustic domain length along the z direction, M is the local Mach number, c is the local sound speed, p_∞ the asyntotic nominal pressure. It is reminded that Poinsot [5] obtained oscillating solutions for $\sigma = 0.58$, and good results for $\sigma = 0.25$, that is close to the theoretical value of Rudy [2]. For reacting flows, we stress the importance of taking into account the effect of the local heat $\dot{Q}$ released by chemical reactions in the evaluation of the incoming wave, as firstly observed in [9], to avoid unphysical pressure increase at the outlet when reacting pockets pass through.

When forcing the wave L_1 at the outlet with $\sigma > 0$, the outlet becomes partially non-reflecting, its response having a characteristic time

$$\tau \sim \frac{2L_z}{\sigma c \left(1 - M^2\right)}. \tag{1.14}$$

Outgoing waves with frequencies higher than $1/\tau$ will cross the boundary without reflections, while those with lower frequencies will be reflected.

It is finally observed that a nil normal gradient is assumed for each of the diffusive fluxes, i.e., for τ_{rz} and $\tau_{\theta z}$ (momentum diffusion), q_z (heat diffusion), J_z (mass diffusion). Furthermore, to avoid flow reversal and consequent numerical instabilities, if the velocity $u_z < 0$ also a nil normal gradient is assumed for the stress τ_{zz} and furthermore, all the outgoing waves that would become incoming have to be forced to be nil ($L_1 = L_2 = L_3 = L_4 = L_{s_i} = L_6 = 0$).

At a supersonic inflow, the amplitude of all waves have to be specified. At a subsonic inflow, there are $4 + N_s$ (N_s being the number of transported species) incoming waves and just one outgoing. According to our experience, inlet partially non-reflecting boundary conditions are mandatory when using high-order spatial schemes. Moreover, they are particularly important in simulations dealing with flame flashback phenomena: using a reflecting boundary will result in unphysical pressure increase at the inlet when the flame tends to move towards the inlet, thus damping the flashback [10].

The same relaxation procedure adopted to model partially non-reflecting outflows is adopted at inlets. Hence, for an inlet boundary located on the left side of the computational domain (the stream flows from left to right) the outgoing L_1 can be computed from the inner flowfield, while the amplitudes of the incoming waves are modelled as [11, 12]

$$L_2^{target} = -\sigma_T \rho R_g u_z \frac{T - T_\infty}{L_z} \tag{1.15}$$

$$L_3^{target} = \sigma_u u_z \frac{u_r - u_{r_\infty}}{L_z} \tag{1.16}$$

$$L_4^{target} = \sigma_u u_z \frac{u_\vartheta - u_{\vartheta\infty}}{L_z} \tag{1.17}$$

$$L_5^{target} = \sigma_u \rho c^2 \frac{u_z - u_{z_\infty}}{L_z} \tag{1.18}$$

$$L_{s_i}^{target} = \sigma_{Y_i} u_z \frac{Y_i - Y_{i_\infty}}{L_z}, \tag{1.19}$$

where different relaxation constants σ can be assumed, and the asyntotic desired inlet values are specified; L_z is the acoustic length in the z direction. It is observed that the inlet conditions currently implemented and tested assumed no-NSCBC treatment for mass fractions for stability reasons: this means that Y_i are simply fixed at inlet, the associated transport equations are not solved, $L_{s_i} = 0$, and hence flames cannot pass through the inlet boundary.

Also in this case, a nil normal gradient is assumed for each of the diffusive fluxes, i.e., for τ_{rz} and $\tau_{\theta z}$ (momentum diffusion), q_z (heat diffusion), J_z (mass diffusion). Furthermore, to avoid flow reversal and consequent

numerical instabilities, if the velocity $u_z < 0$ also a nil normal gradient is assumed for the stress τ_{zz} and furthermore, all the incoming waves that would become outgoing have to be forced to be nil ($L_2 = L_3 = L_4 = L_5 = L_{s_i} = L_6 = 0$).

1.3 Some Notes on the Outflow for Real Gas Flows

The non-reflecting outflow boundary condition already implemented in the HeaRT code is extended to real gas trans- and supercritical flows. There is a few literature on this topics: in fact, only three works provide some details about characteristic boundary conditions extension to real gases, the first being the work of Okong'o and Bellan [8] (used to derive the correction factors Rg_1 and Rg_2 in Eqn. (1.5)), the other two being the works of Coussement [13] and Petit [14]. Besides there are other works that provide some tips about the outflow boundary condition for transcritical and supercritical flows.

Considering the numerical simulations of real gases available in literature and focusing on the outflow boundary conditions adopted, such simulations can be gathered in four groups:

1. simulations dealing with supersonic flows, that do not provide information on how to define the incoming pressure wave (1.13) since it is not required [8];

2. simulations with sufficiently long domain in the streamwise direction, experiencing no or weak eddies (negligible curvature) crossing the non-reflecting outflow [15, 16, 17];

3. simulations with short domain in the streamwise direction, assuming a simple pressure outlet (pressure fixed at the exit) with or without a sponge layer to damp fluctuations close to the exit [18, 19, 14, 20];

4. simulations with three-dimensional treatment of waves in the Navier-Stokes Characteristic Boundary Conditions approach [7] extended to real gases, suggesting an expression for the relaxation parameter σ in Eqn. (1.13) in case of transcritical flows [13] or using the transverse relaxation parameter (required in the original framework to specify the asimptotic transverse behaviour of the flow at the exit) as a transverse damping parameter (to damp curvature effects at the exit) [14].

Reckoning on this, it can be concluded that in numerical simulation of transcritical and supercritical flows the curvature effects onto the NSCBC-1D subsonic outflow boundary are expected to be amplified by the much higher momentum with respect to the subcritical regime. In general, the best solution is to couple a sufficiently long domain in the streamwise direction with a NSCBC strategy. The adoption of the NSCBC-3D strategy with a transverse damping parameter or NSCBC-1D with a specific expression for the relaxation parameter σ in Eqn. (1.13) may be of help in short computational domains when eddies cross the outlet. It is observed that regions where flames cross the boundary produce less problems than simple mixing since hot combustion products are close to an ideal gas also at high pressure.

The correction factors Rg_1 and Rg_2 in Eqn. (1.5) were implemented in the NSCBC-1D boundary treatment and the standard expression for the incoming pressure wave (1.13) was assumed. Two two-dimensional tests were performed through the code HeaRT:

- non-reacting spatial shear-layer (400×400 nodes uniformly distributed from 0 to 3 mm in the streamwise direction, and stretched from -2 to 2 mm in the crosswise direction): a central nitrogen jet at 5 m/s and 130 K surrounded by a hydrogen coflow at 120 m/s and 270 K, at 40 bar (the inlet profiles come from the simulation of an associated temporal shear-layer, and hence, they already show turbulent mixing);

- reacting spatial shear-layer (406×427 nodes uniformly distributed from 0.3 to 5.3 mm in the streamwise direction, and stretched from -2.47 to 2.06 mm in the crosswise direction): a central methane jet at 100 m/s and 300 K surrounded by an oxygen coflow at 25 m/s and 300 K, at 150 bar (the inlet profiles come from the simulation of an associated temporal shear-layer, and hence, they already show turbulent mixing and combustion).

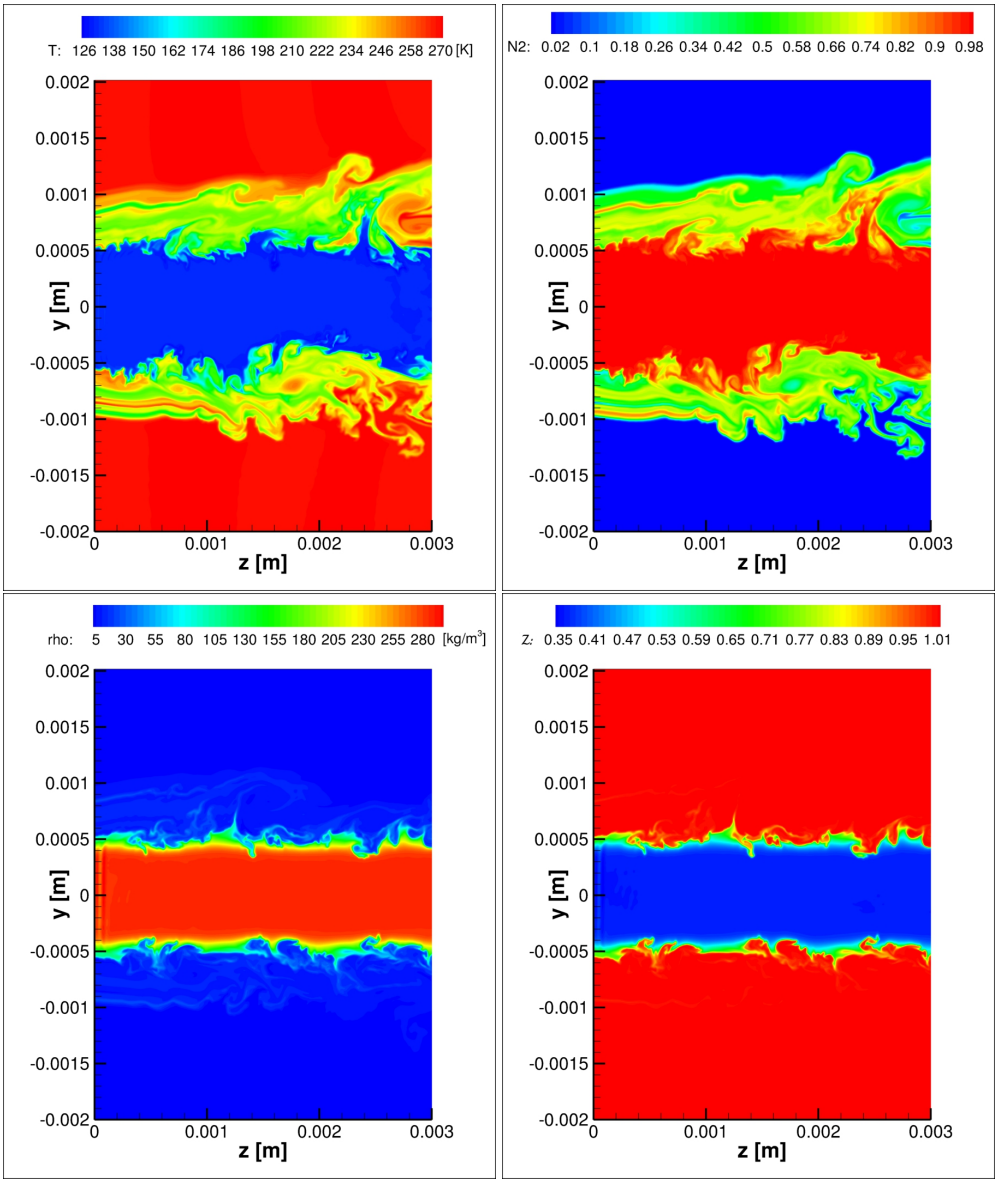

Figura 1.2: Instantaneous distribution of temperature, N_2 mass fraction, density and compressibility factor for the non-reacting shear-layer.

Outflow non-reflecting boundary conditions with $\sigma = 0$ were assumed along the bottom and top boundaries of the non-reating shear-layer; adiabatic no-slip walls were assumed for the same boundaries in the second simulation; the inlet boundary is reflecting (quantities imposed and nil pressure gradient) and the outlet is partially non-reflecting with $\sigma = 0.27$ in both cases. Instantaneous distribution of temperature, N_2 mass fraction, density and compressibility factor for the non-reacting shear-layer are shown in Fig. 1.2. Instantaneous distribution of temperature, H_2 mass fraction, density and compressibility factor for the reacting shear-layer are shown in Fig. 1.3.

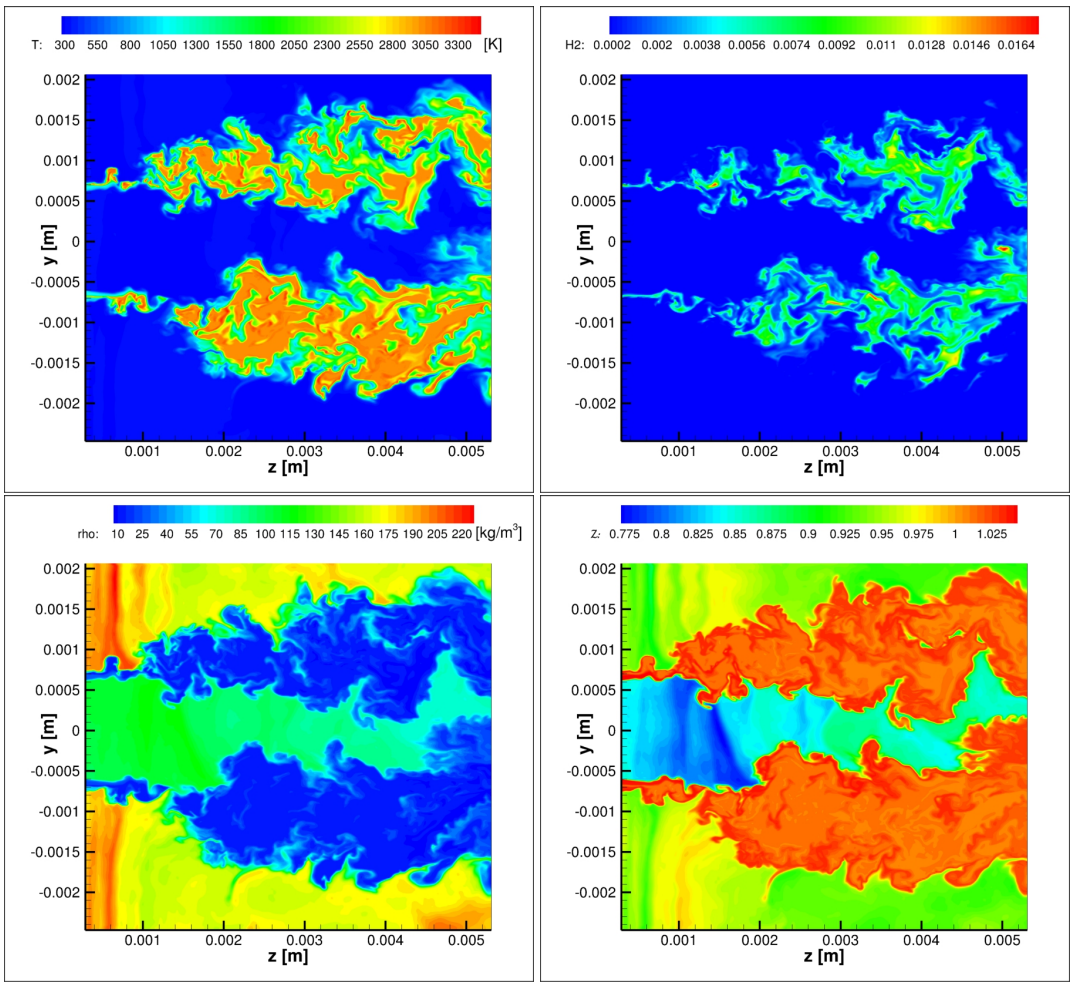

Figura 1.3: Instantaneous distribution of temperature, H_2 mass fraction, density and compressibility factor for the reacting shear-layer.

2 Numerical Schemes for Real Gas Applications

Attention is here focused on the discretization of the convective terms of the transport equations in their conservative formulation or alternative strategies involving artifical diffusivity. The objective is to adopt a robust and accurate numerical scheme able to solve problems involving large spatial gradients, contact discontinuities, variable Mach number, typically found in real gas applications.

2.1 Localized Artificial Diffusion and Pressure Evolution Equation

A fully conservative (FC) scheme formulation of the governing equations has been used for most simulations of supercritical jet mixing flows. It is well known that spurious oscillations are generated at interfaces when a (fully conservative) FC form of the governing equations is used for simulations of compressible multi-component flows and especially in the case of supercritical flows [21]. It occurs because of different thermodynamic properties in each fluid, e.g., different specific heat ratios between two fluids. The spurious oscillations may harm the prediction accuracy of flow fields such as turbulence or acoustics, as well as computational stability, especially when high-order schemes are used. Instead of enforcing the total energy equation, for the simulation of supercritical jet flows, a solution is to solve a pressure evolution equation. This enables to maintain pressure equilibrium easily and can be used with any type of equation of state without major modifications [22]:

$$\frac{\partial p}{\partial t} + \boldsymbol{u} \cdot \nabla p = -\rho c^2 \nabla \cdot \boldsymbol{u} + \frac{\alpha_p}{c_v \beta_T} \left[\frac{1}{\rho} \left(\tau : \boldsymbol{E} - \nabla q \right) \right] + \sum_{i=1}^{N} \left(\frac{\partial p}{\partial Yi} \right)_{\rho,e} \left[\frac{1}{\rho} \nabla \cdot (\rho D_i) \nabla Y_i \right], \tag{2.1}$$

where $\boldsymbol{E}$ is the strain rate tensor, the symmetric part of $\nabla \boldsymbol{u}$.

Following the approach of [22], explicit numerical diffusion terms are usually introduced to the governing equations to maintain stable computations when central difference schemes are used. If the numerical diffusion terms are inconsistently introduced, they may disturb the velocity and pressure equilibriums at inviscid interfaces, producing severe spurious oscillations. In fact, when a cryogenic jet is injected into a chamber at room temperature, interfacial regions with high density or temperature ratio exist between the jet and the chamber fluids. A numerical diffusion term for the mass conservation equation using the density gradient is introduced

$$\frac{\partial \rho}{\partial t} + \nabla \cdot (\rho(u)) = \nabla \cdot (\varphi_\rho \nabla \rho), \tag{2.2}$$

with

$$\varphi_\rho = C_\rho \frac{c}{\rho} \overline{\left| \sum_{l=1}^{S} \frac{\partial^4 \rho}{\partial x_l^4} \Delta_l^5 \right|}, \tag{2.3}$$

S being the number of dimensions. The overbar indicates a truncated Gaussian filter. The last term in Eqn. 2.2 must be consistent with the term $\nabla \cdot (\varphi_\rho \nabla \rho Y_i)$ added to the right hand side of species equations.

This approach has been validated in [22] for simulating cryogenic jet mixing under supercritical pressures using high order schemes. The consistent numerical diffusion term for the species-mass equation is also built and the artificial diffusion coefficient is introduced to avoid mass fraction/temperature oscillations in multi-species flow cases.

Although this method is valid for the treatment of material discontinuities, avoiding the formation of spurious oscillations, it was preferable to introduce into the HeaRT code a Riemann partial solver called $AUSM^+ - up$ for its simpler implementation and effectiveness.

2.2 The $AUSM^+ - up$ Numerical Scheme

The $AUSM$ (Advection Upstream Splitting Method) family scheme has been selected [23, 24, 25], and in particular the latest release $AUSM^+ - up$ [26]. This numerical scheme has been selected because it features these characteristics:

1. exact capturing of a contact discontinuity;
2. exact capturing of a normal shock discontinuity with an entropy-satisfying property;
3. positivity preserving property;
4. solution free of carbuncle phenomenon;
5. accurate solution of slowly moving contact discontinuities;
6. smooth transition through the sonic speed;
7. maintaining convergence and accuracy in a Mach-number-independent fashion.

In the referenced literature the reader can found more details than those in the present algorithm scheme. For simplicity, the $AUSM^+ - up$ numerical scheme is described considering the one-dimensional inviscid transport equations:

$$\frac{\partial \boldsymbol{Q}}{\partial t} + \nabla \cdot \boldsymbol{F} = 0, \tag{2.4}$$

where $\boldsymbol{Q} = \{\rho, \rho u, \rho \mathcal{U}, \rho Y_i\}^T$ is the vector of transported quantities, $\boldsymbol{F} = \{\rho u, \rho uu + p, \rho u\mathcal{H}, \rho u Y_i\}^T$ is the flux vector, ρ being the density, u the velocity, $\mathcal{U}$ and $\mathcal{H}$ the total energy and enthalpy (the total quantities include the kinetic energy $u^2/2$), Y_i the individual species mass fractions.

As common in all $AUSM$ schemes, the inviscid flux is splitted into convective and pressure fluxes:

$$\boldsymbol{F} = \begin{Bmatrix} \rho u \\ \rho uu + p \\ \rho u\mathcal{H} \\ \rho u Y_i \end{Bmatrix} = \rho u \begin{Bmatrix} 1 \\ u \\ \mathcal{H} \\ Y_i \end{Bmatrix} + \begin{Bmatrix} 0 \\ p \\ 0 \\ 0 \end{Bmatrix} = \dot{m}\boldsymbol{\psi} + \boldsymbol{P} \tag{2.5}$$

where $\dot{m} = \rho u$ is the scalar mass flux with its own sign that convectively transports the vector quantity $\boldsymbol{\psi}$. According to the $AUSM$ method the numerical flux at the interface I is written as

$$\boldsymbol{f}_I = \dot{m}_I \boldsymbol{\psi}_{L/R} + \boldsymbol{P}_I, \tag{2.6}$$

where $\boldsymbol{\psi}_{L/R}$ are the left and right states of the vector quantity $\boldsymbol{\psi}$ at the interface I, with

$$\boldsymbol{\psi}_{L/R} = \begin{cases} \boldsymbol{\psi}_L & \text{if } \dot{m}_I > 0 \\ \boldsymbol{\psi}_R & \text{otherwise.} \end{cases} \tag{2.7}$$

For a collocated formulation, at first order such quantities can simply be the values at the computational nodes at the left and right of the interface where the flux is calculated. In the code HeaRT, a $5^{th} - 3^{rd}$ order $WENO$ interpolation procedure is adopted to estimate the left and right states, the order of accuracy depending on a local sensor.

2.2.1 The Mass Flux

According to the $AUSM^+ - up$ numerical scheme the mass flux at the interface I is

$$\dot{m}_I = a_I \mathcal{M}_I \begin{cases} \rho_L & \text{if } \mathcal{M}_I > 0 \\ \rho_R & \text{otherwise.} \end{cases} \tag{2.8}$$

where a_I and $\mathcal{M}_I = u_I/a_I$ are, respectively, the speed of sound and the Mach number (at the interface I) that have to be calculated according to a specific procedure. In particular, in this work the simplest choice for the interface speed of sound a_I is adopted, i.e.,

$$a_I = \frac{a_L + a_R}{2}, \tag{2.9}$$

although more complex definitions can be chosen for specific problems [1]. It is observed that the interface speed of sound is uniquei, i.e., its left and right states are not used anymore in the algorithm: this strategy is believed (by the authors of this report) to be the key to successfully solve contact discontinuities. The interface Mach number $\mathcal{M}_I$ is estimated through the following procedure.

- The left and right Mach number is firstly defined: $\mathcal{M}_{L/R} = u_{L/R}/a_I$.
- The following split functions are computed ($\mathcal{M}$ will be $\mathcal{M}_L$ or $\mathcal{M}_R$):

$$\mathbb{M}^{\pm}_{(1)}(\mathcal{M}) = \frac{\mathcal{M} \pm |\mathcal{M}|}{2} \tag{2.10}$$

$$\mathbb{M}^{\pm}_{(2)}(\mathcal{M}) = \pm\frac{(\mathcal{M} \pm 1)^2}{4} \tag{2.11}$$

$$\mathbb{M}^{\pm}_{(4)}(\mathcal{M}) = \begin{cases} \mathbb{M}^{\pm}_{(1)} & \text{if } |\mathcal{M}| \geq 1 \\ \mathbb{M}^{\pm}_{(2)} \cdot \left(1 \mp 16\beta \cdot \mathbb{M}^{\mp}_{(2)}\right) & \text{otherwise.} \end{cases} \tag{2.12}$$

  where $\beta = 1/8$ is assumed. The number written as pedex of the split functions are the degree of the polynomial functions adopted.

- A pressure diffusion term is defined to enhance calculations of low Mach number or multi-phase flows,

$$M_p = -\frac{K_p}{f_a} \cdot Max\left[1 - \sigma\overline{\mathcal{M}}^2; 0\right] \cdot \frac{p_R - p_L}{\rho_I a_I^2}, \tag{2.13}$$

  where

$$\overline{\mathcal{M}}^2 = \frac{\mathcal{M}_L^2 + \mathcal{M}_R^2}{2} \tag{2.14}$$

$$\rho_I = \frac{\rho_L + \rho_R}{2}. \tag{2.15}$$

  In this expression there are two constants. The first one is $K_p \in [0; 1]$ that is assumed to be 0.25. The second one is $\sigma \in [1/4; 1]$, that is assumed to be 1. The smaller σ becomes, the smoother the result is [2].

  It is observed that, due to the term $Max\left[1 - \sigma\overline{\mathcal{M}}^2; 0\right]$, the pressure diffusion term M_p is activated only when $1 - \sigma\overline{\mathcal{M}}^2 > 0$, i.e., $\overline{\mathcal{M}}^2 \leq 1/\sigma$. Since the constant $\sigma \in [0; 1]$, it follows that σ is effective only in $\overline{\mathcal{M}} > 1$ regions, where $1 \leq \overline{\mathcal{M}}^2 \leq 1/\sigma$.

  The suffix "p" in the name of the scheme comes from including the M_p pressure diffusion term. At low Mach numbers, the term M_p may not provide sufficient dissipation since $(p_R - p_L)$ will be small and in fact of the order $O(\mathcal{M}^2 \ll 1$. Including the scaling function f_a for the speed of sound, an extension for all speeds is provided. The f_a function is a sound speed scaling factor, that will be adopted also in the pressure flux definition and that makes the $AUSM^+ - up$ numerical scheme applicable for all speeds (from low to high Mach number flows). It is defined as

$$f_a = \mathcal{M}_0 \cdot (2 - \mathcal{M}_0) \in [0; 1] \tag{2.16}$$

$$\mathcal{M}_0^2 = Min\left[1; Max\left(\overline{\mathcal{M}}^2, \mathcal{M}_\infty^2\right)\right] \in [0; 1]. \tag{2.17}$$

[1] To exactly resolve a normal shock between two discontinuous states, the author in [26] suggests to define $a_I = Min\left[\hat{a}_L; \hat{a}_R\right]$, where $\hat{a}_L = a^{*^2}/Max\left[a^*; u_L\right]$ and $\hat{a}_R = a^{*^2}/Max\left[a^*; -u_R\right]$, a^* being the critical speed of sound evaluated when the local Mach number is unity, i.e., $a^{*^2} = 2(\gamma - 1)\mathcal{H}/(\gamma + 1)$ (for an ideal gas, γ being the specific heat ratio). With this choice, a stationary shock is exactly preserved.

[2] The minimum value of σ for shock capturing is $\sigma_{min} = 2/\left[1 + \left(\mathcal{M}_L a_L/a_L^*\right)^4\right]$.

- The interface Mach number $\mathcal{M}_I$ is then calculated as

$$\mathcal{M}_I = \mathbb{M}^+_{(4)}(\mathcal{M}_L) + \mathbb{M}^-_{(4)}(\mathcal{M}_R) + M_p. \tag{2.18}$$

  If $\mathcal{M}_L = \mathcal{M}_R = \mathcal{M}_I$, it is observed that $\mathbb{M}^+_{(4)}(\mathcal{M}_I) + \mathbb{M}^-_{(4)}(\mathcal{M}_I) = \mathcal{M}_I$.

- Finally, considering Eqns. (2.6) and (2.7), the mass flux at interface I in Eqn. (2.8) is calculated and implemented as:

$$\dot{m}_I = \frac{a_I}{2} \cdot [\mathcal{M}_I \cdot (\rho_L + \rho_R) + |\mathcal{M}_I| \cdot (\rho_L - \rho_R)] \tag{2.19}$$

2.2.2 The Other Scalar Fluxes

Once calculated the mass flux $\dot{m}_I$ by means of Eqn. (2.19), considering Eqns. (2.6) and (2.7) the fluxes of energy and individual species mass fractions at the interface I are calculated as:

$$\dot{m}_I \mathcal{H}_I = \frac{1}{2} \cdot [\dot{m}_I \cdot (\mathcal{H}_L + \mathcal{H}_R) + |\dot{m}_I| \cdot (\mathcal{H}_L - \mathcal{H}_R)] \tag{2.20}$$

$$\dot{m}_I Y_{i_I} = \frac{1}{2} \cdot [\dot{m}_I \cdot (Y_{i_L} + Y_{i_R}) + |\dot{m}_I| \cdot (Y_{i_L} - Y_{i_R})]. \tag{2.21}$$

2.2.3 The Momentum Flux

Once calculated the mass flux $\dot{m}_I$ by means of Eqn. (2.19), considering Eqns. (2.6) and (2.7) the flux of momentum at the interface I is calculated as

$$\dot{m}_I u_I + p_I = \frac{1}{2} \cdot [\dot{m}_I \cdot (u_L + u_R) + |\dot{m}_I| \cdot (u_L - u_R)] + p_I, \tag{2.22}$$

where the pressure flux p_I is calculated through the following procedure.

- The following split functions are computed ($\mathcal{M}$ will be $\mathcal{M}_L$ or $\mathcal{M}_R$):

$$\mathbb{P}^{\pm}_{(5)}(\mathcal{M}) = \begin{cases} \frac{1}{\mathcal{M}} \cdot \mathbb{M}^{\pm}_{(1)} & \text{if } |\mathcal{M}| \geq 1 \\ \mathbb{M}^{\pm}_{(2)} \cdot \left[\pm 2 - \mathcal{M} \mp 16\alpha \cdot \mathcal{M} \cdot \mathbb{M}^{\mp}_{(2)}\right] & \text{otherwise.} \end{cases} \tag{2.23}$$

  The constant $\alpha \in [-3/4; 3/16]$ is obtained through

$$\alpha = \frac{3}{16}\left(-4 + 5 f_a^2\right). \tag{2.24}$$

  If $\mathcal{M}_L = \mathcal{M}_R = \mathcal{M}_I$, it is observed that $\mathbb{P}^+_{(5)}(\mathcal{M}_I) + \mathbb{P}^-_{(5)}(\mathcal{M}_I) = 1$.

- A velocity difference diffusion term P_u is defined to enhance calculations of low Mach number or multi-phase flows,

$$P_u = -K_u \cdot \mathbb{P}^+_{(5)}(\mathcal{M}_L) \cdot \mathbb{P}^-_{(5)}(\mathcal{M}_R) \cdot (\rho_L + \rho_R) \cdot (u_R - u_L) \cdot f_a a_I, \tag{2.25}$$

  where the constant $K_u \in [0; 1]$ is assumed to be 0.75. The coefficient $\mathbb{P}^+_{(5)}(\mathcal{M}_L) \cdot \mathbb{P}^-_{(5)}(\mathcal{M}_R)$ simply switches off P_u as the flow becomes supersonic, resulting in one-sided upwinding. The suffix "u" in the name of the scheme comes from including the P_u velocity diffusion term. The f_a function is a sound speed scaling factor, already introduced in the pressure diffusion term M_p, that makes the $AUSM^+ - up$ numerical scheme applicable for all speeds (from low to high Mach number flows).

- The interface pressure flux p_I is then calculated as

$$p_I = \mathbb{P}^+_{(5)}(\mathcal{M}_L) \cdot p_L + \mathbb{P}^-_{(5)}(\mathcal{M}_R) \cdot p_R + P_u. \tag{2.26}$$

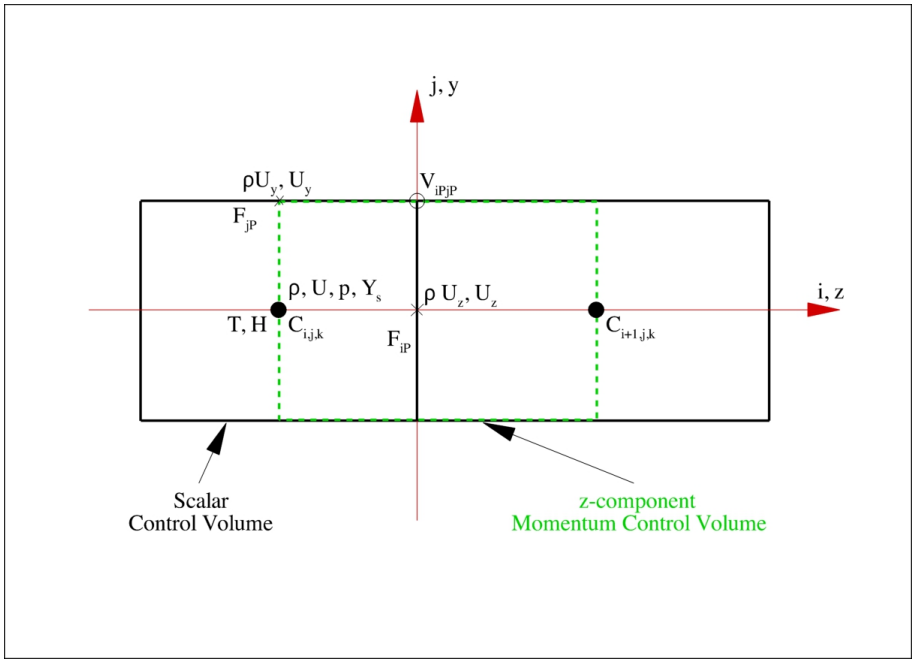

Figura 2.1: Sketch of the variable location in the staggered formulation adopted in the code HeaRT. The control volumes of scalar quantities (black) and of ρU_z momentum component (green) are shown.

Concerning the ”all speed” feature of the scheme, it is reminded that standard methods developed for compressible flows do not work properly in low Mach number simulation, resulting in convergence and accuracy problems. The convergence problem comes from the disparity of convective and acoustic speeds moving towards low Mach numbers. This problem is commonly solved by modifying the structure of the eigenvalues through preconditioning of the time derivative term. The accuracy problem comes from the discretization; in fact, when decreasing the Mach number of the flow, the pressure term dominates (small perturbations in the pressure field results in zeroth-order changes in the velocity field) and proper scaling of pressure differences must be reflected in the numerical scheme to avoid inaccuracy and corruption of the solution. By introducing the sound speed scaling factor f_a the current scheme will hold its accuracy consistently for computations of low Mach number flows, thus exhibiting a ”for all speeds” feature.

2.2.4 Staggered Formulation

When a staggered formulation of the transported quantities is adopted, the scalars are located at the center of the computational cell, while the velocity components are located at the center of the faces of the cell. Hence, there will be four different control volumes to be managed. A sketch of the control volumes and variable location is shown in Fig. 2.1.

When a flux splitting method is adopted in a staggered formulation, the left and right states cannot be calculated for every quantity at every interfaces, since some quantities are already well known at a specific interface (depending on the control volume under consideration) due to the staggered formulation. Being more specific:

- For the mass flux, the velocity at the interface is unique, i.e., $u_L = u_R = u_I = u$, since u is located at the center of the interface for the scalar control volume. Hence, $\mathcal{M}_L = \mathcal{M}_R = \mathcal{M}_I$, and this completely avoids the calculation of the split functions for the mass flux since $\mathbb{M}^+_{(4)}(\mathcal{M}_I) + \mathbb{M}^-_{(4)}(\mathcal{M}_I) = \mathcal{M}_I$.

- For the normal component of momentum flux, instead, there will be u_L and u_R, and hence, $\mathcal{M}_L$ and $\mathcal{M}_R$. In this case, since the pressure is exactly known at the interface of momentum control volume, $p_L = p_R = p_I = p$ thus resulting in $M_p = 0$ and a simpler expression for the velocity difference diffusion term (2.25).

Here, also some particular solutions adopted in the staggered formulation of the code HeaRT, that increased accuracy with respect to other alternative solutions, are reported:

1. The stencil of enthalpy calculated from transported quantities ($\mathcal{H} = \mathcal{U} + p/\rho$) is passed to the $WENO$ interpolation routine to calculate $\mathcal{H}_L$ and $\mathcal{H}_R$.

2. In multi-dimension, for the normal flux of each momentum transport equation (e.g., $\rho U_z U_z + p$ for the z-component momentum equation) the stored velocity (e.g., U_z) is passed to the $WENO$ interpolation routine (from face to center) to calculate the left and right states (e.g., U_{z_L} and U_{z_R}). Considering that the density is already known at the location of the momentum control volume interface, the normal flux is calculated as
$$\rho_I U_{z_I} U_{z_I} + p_I = \frac{\rho_I a_I}{2} \cdot [\mathcal{M}_I \cdot (U_{z_L} + U_{z_R}) + |\mathcal{M}_I| \cdot (U_{z_L} - U_{z_R})] + p_I, \tag{2.27}$$
It is remarked that both ρ_I and a_I come directly from the stored flowfield and not from Eqns. (2.9) and (2.15). This implies that the term $\rho_L + \rho_R$ in Eqn. (2.25) becomes $2\rho_I$.
For the cross flux $\rho U_z U_y$, it is observed that the velocity U_y is already known at the center of the interface normal to y of the scalar control volume. Hence, no left and right states are calculated: U_y at the vertex V_{iPjP} will be obtained by a simple linear interpolation between the values from two adjacent cells. It follows that the Mach number $\mathcal{M}_I = U_y\big|_{V_{iPjP}} / a_I$, with a_I coming from Eqn. (2.9), is unique, i.e., no left and right states are defined; hence, as it was already observed for the scalars fluxes, also in this case the calculation of the split functions is completely avoided. The cross flux is thus calculated as
$$\rho_I U_{z_I} U_{y_I} = \frac{a_I}{2} \cdot \{\mathcal{M}_I \cdot [(\rho U_z)_L + (\rho U_z)_R] + |\mathcal{M}_I| \cdot [(\rho U_z)_L - (\rho U_z)_R]\}, \tag{2.28}$$
where the $(\rho U_z)_{L/R}$ have been obtained passing the ρU_z stencil to the $WENO$ routine (from face to vertex, i.e., from center to face). This choice reduces the number of low order (linear) interpolations and reduces wiggles.

2.2.5 Numerical Tests

The $AUSM^+ - up$ numerical scheme implemented in the code HeaRT has been extensively validated and tested.

- **The 1D-SOD problem**: the SOD shock tube problem [27] is commonly used to test the accuracy of numerical schemes. The test done here consists of a one-dimensional real gas (the Peng-Robinson equation of state was assumed) Riemann problem having nil velocity, uniform temperature (300 K), uniform O_2 concentration, 150 bar and 15 bar on the left and right side of $z = 0.05$ m, respectively. With this pressure jump, the density is nearly 203 kg/m^3 on the left and 19.46 kg/m^3 on the right. The computational domain has 100 grid nodes uniformly distributed over a length of 1 cm. From the initial condition, the flow evolves experiencing a rarefaction wave (on the left of the initial discontinuity), a contact and a shock discontinuity moving towards the right of the computational domain. Analytical solution of the inviscid Euler equations can be obtained and compared to numerical results. Time evolution of pressure and density are shown in Figs. 2.2 and 2.3; the analitical solution (not shown) is nearly superimposed to the numerical predictions. It is noted that the pressure correctly does not change across the contanct discontinuity.

  Different implementations of the $AUSM^+ - up$ scheme are compared in Fig. 2.4 (it is observed that these tests were done with the ideal gas equation of state): v5 refers to the version that builds the left and right states of enthalpy $\mathcal{H}_{L/R}$ by using the associated states of total energy $\mathcal{U}_{L/R}$, pressure $p_{L/R}$ and density $\rho_{L/R}$, i.e., $\mathcal{H}_{L/R} = \mathcal{U}_{L/R} + p_{L/R}/\rho_{L/R}$; v5b refers to the version that builds the left and right states of enthalpy $\mathcal{H}_{L/R}$ directly from the $WENO$ routines that receive as input the enthalpy built from the field quantities, i.e., $\mathcal{H} = \mathcal{U} + p/\rho$; v5c refers to the version that computes the normal flux of each momentum transport equation according to Eqn. (2.27), where only the stored primitive variable velocity has been passed to the $WENO$ routine (not the momentum ρu); v6 refers to a version where the left and right

states were calculated for every quantities at every interface by using low order interpolations. The best result is obtained through the implementation v5c. Besides this, it is observed that in general the ideal gas solution experiences less wiggles than the real gas one.

Figure 2.5 compares the solutions obtained by means of the best implementation of the $AUSM^+ - up$ scheme adopting the $WENO$ ($5^{th} - 3^{rd}$ order) and QUICK (3^{rd} order) interpolation procedures to build the left and right states of required quantities. The solution obtained with the $WENO$ interpolation is clearly better.

Figure 2.6 reports the same simulation over a longer (0.5 m vs 0.1 m) computational domain with 500 (vs 100) grid nodes, showing how the discontinuities are correctly transported.

The above simulations were performed with a $CFL = 0.25$ for both convective and viscous terms. The robustness of the scheme was also tested and proved by increasing the CFL up to 0.65: solution overlaps at different time steps with that at $CFL = 0.25$ without showing additional wiggles. At $CFL = 0.75$ the simulation diverges after 38 time steps.

- **Still and moving contact discontinuity**: the same computational domain of the SOD test was initialized with uniform temperature (300 K), uniform pressure (150 bar), a jump in the species (CH_4 on the left and O_2 on the right). The computational domain has 100 grid nodes uniformly distributed over a length of 1 cm. Two simulations were performed with the real gas Peng-Robinson equation of state, the first with initial velocity field $u = 0$, and the second with $u = 10\,\mathrm{m/s}$. For the still contact discontinuity it is observed that the percent variation of pressure is negligible, as well as temperature and velocity variation (see Fig. 2.7). Previous versions of the $AUSM$ scheme (the first already implemented in the HeaRT code) were not able to maintain the constant pressure, temperature and velocity. For the moving contact discontinuity the percent variation of pressure, as well as temperature and velocity variation are higher than in the previous case, but rapidly decaying and acceptable (see Fig. 2.8).

- **Ideal gas** CH_4/O_2 **temporal shear-layer**: a shear-layer at 1.5 bar between a central jet of methane flowing at 100 m/s and a coflowing stream of oxygen at 25 m/s, both being at 300 K, is simulated with the ideal gas equation of state. The computational domain is two-dimensional with 400 grid nodes uniformly distributed along the streamwise direction and stretched in the crosswise direction. Periodic boundary conditions are assumed in the stream direction, while fully non-reflecting ($\sigma = 0$) boundaries are imposed crosswise. Figure 2.9 shows an instantaneous distribution of CH_4 mass fraction after the roll-up was established. In this simulation the density ranges from $0.96\,\mathrm{kg/m^3}$ in the methane jet to $1.92\,\mathrm{kg/m^3}$ in the oxygen coflow.

Cases	Scalars	Momentum
1	$AUSM/WENO$	$AUSM/QUICK$
2	$AUSM^+ - up/WENO$	2^{nd} order centered
3	$AUSM^+ - up/WENO$	$AUSM^+ - up/WENO$

Tabella 2.1: Numerical schemes compared through the ideal gas temporal shear-layer.

This test case was assumed as a reference test for comparing different numerical schemes. In particular, flowfields and transversal profiles of different quantities obtained through the numerical schemes listed in Table 2.1 were compared. The convective and viscous CFL were 0.2. Results, not reported here, are overlapped; only the solution with the explicit 2^{nd} order centered scheme exhibits some (negligible) oscillations. The scheme referred to as Case 3 was also tested with $CFL = 0.4$: the solution maintained its stability and was overlapped to the others.

- **Real gas** LN_2/GH_2 **temporal shear-layer**: a shear-layer at 40 bar between a central jet of liquid nitrogen at 118 K flowing at 5 m/s and a coflowing stream of gaseous hydrogen at 270 K flowing at 120 m/s,

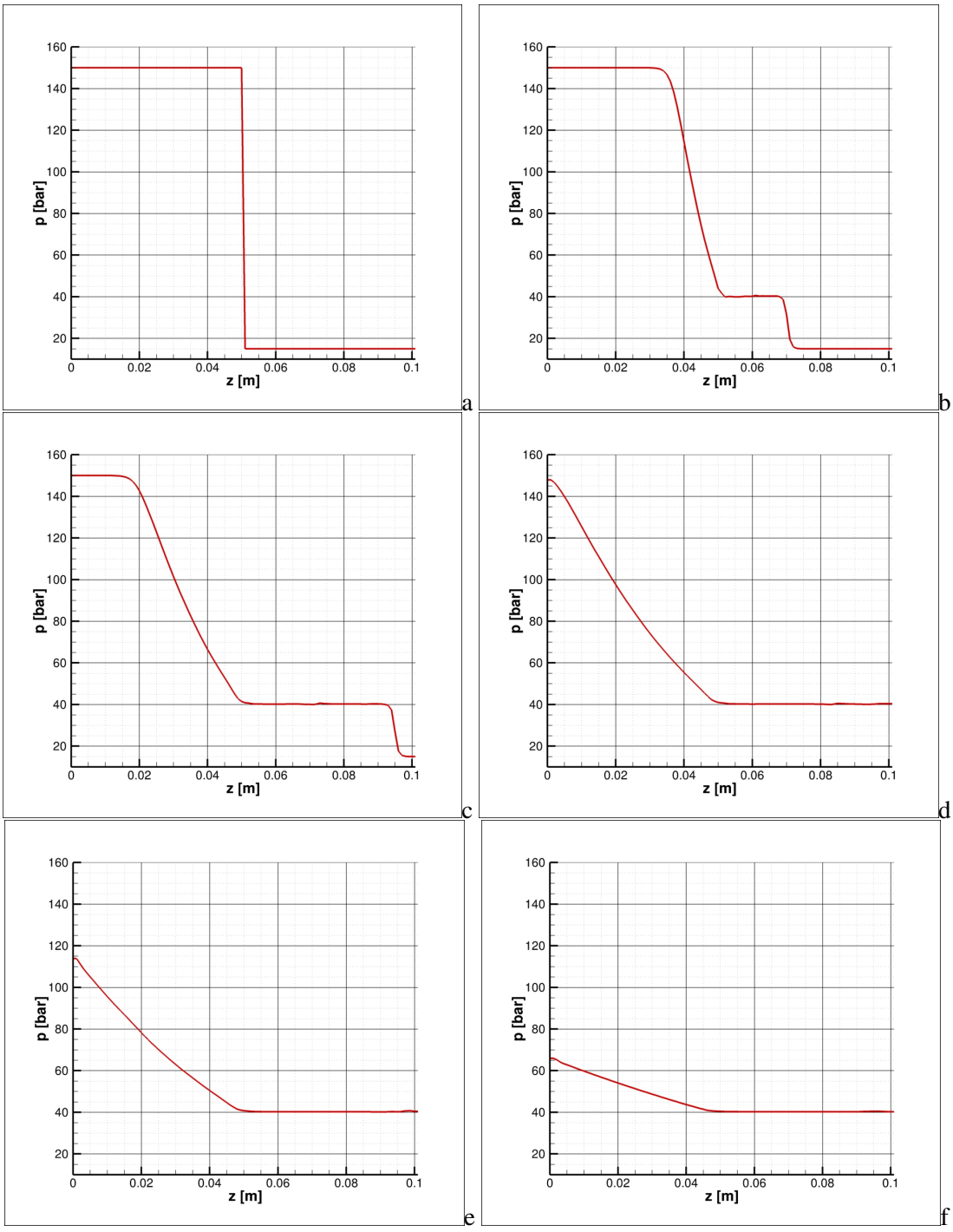

Figura 2.2: Temporal evolution of the pressure in the real gas SOD problem, from its initial field (a) towards its final state. Solution refers to the best implementation of the $AUSM^{+} - up$ scheme adopting the $WENO$ ($5^{th} - 3^{rd}$ order) interpolation.

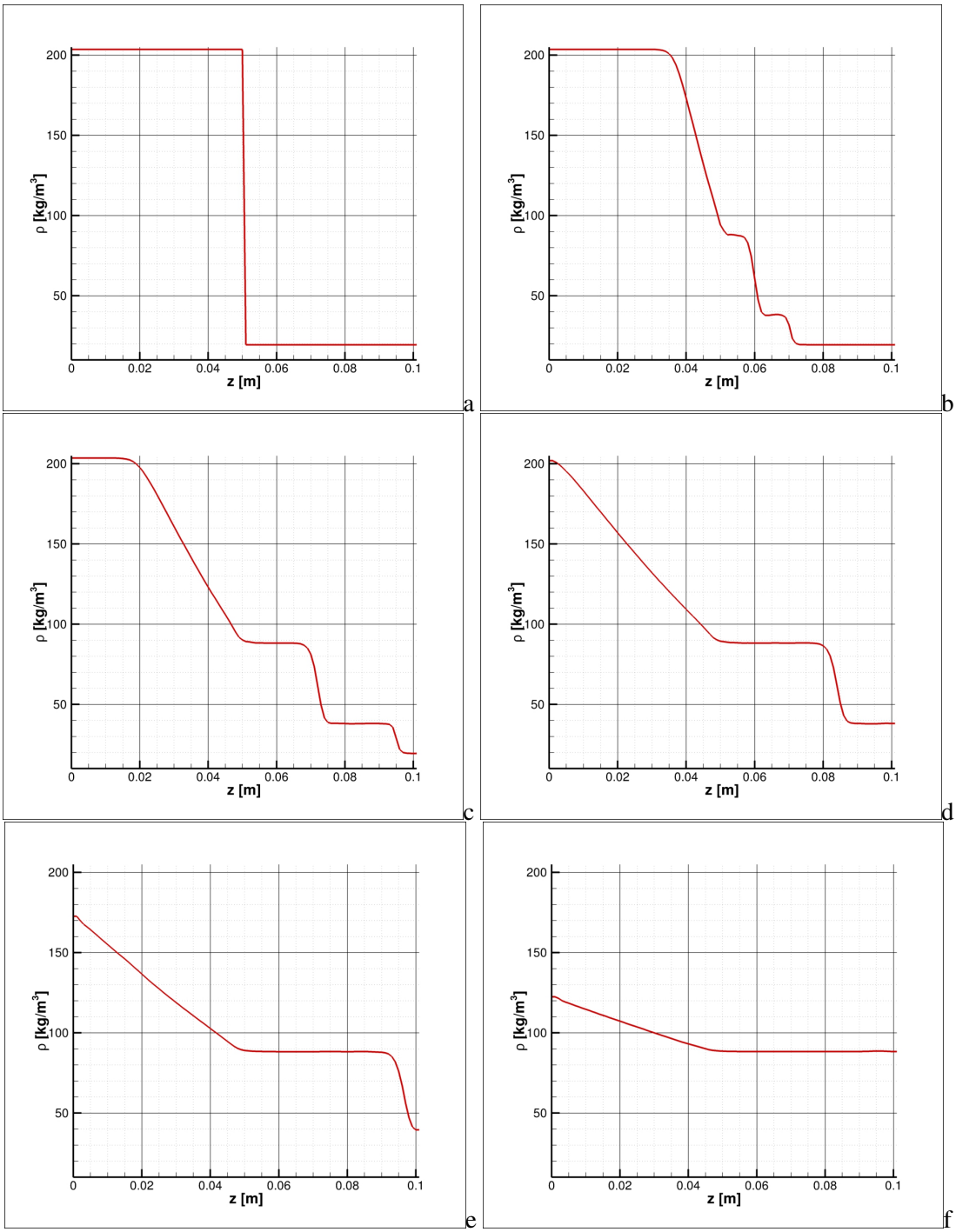

Figura 2.3: Temporal evolution of the density in the real gas SOD problem, from its initial field (a) towards its final state.

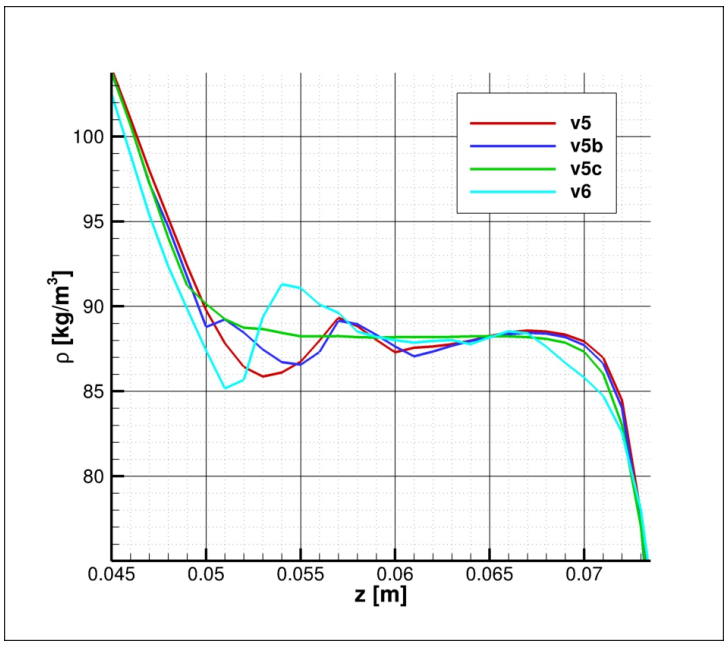

Figura 2.4: Comparison of the ideal gas solutions obtained by means of different implementation of the $AUSM^{+} - up$ scheme in the nearby of the rarefafaction wave origin.

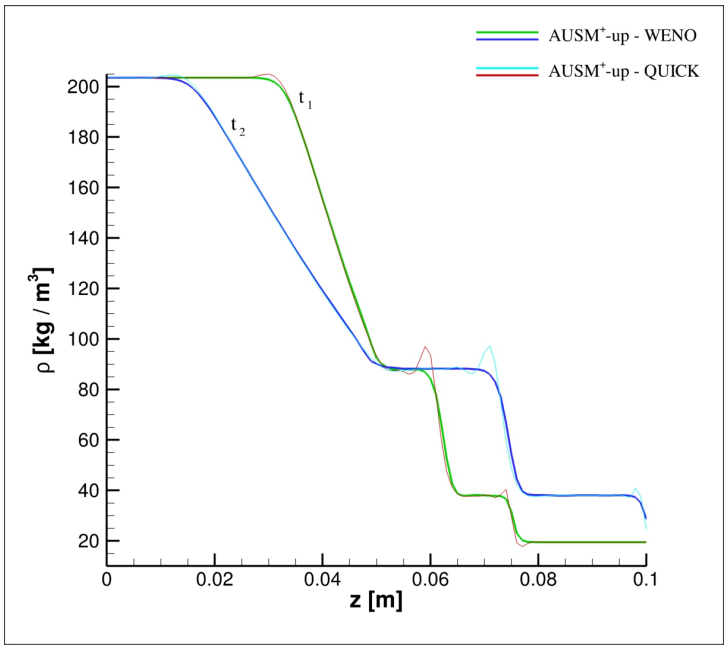

Figura 2.5: Comparison of the real gas solutions obtained by means of the best implementation of the $AUSM^{+} - up$ scheme adopting the $WENO$ ($5^{th} - 3^{rd}$ order) and QUICK (3^{rd} order) interpolations.

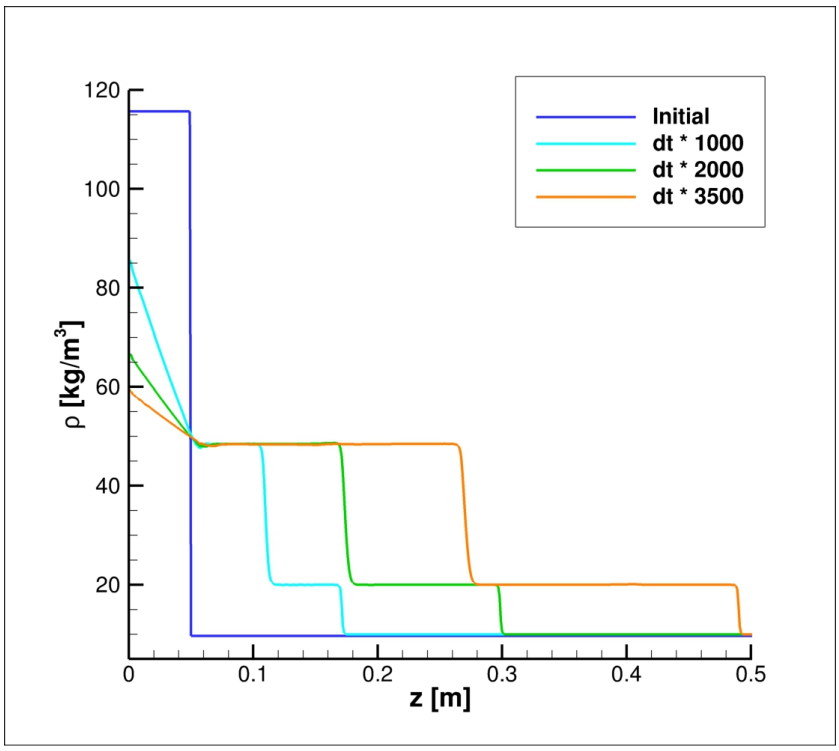

Figura 2.6: Temporal evolution of the density in the real gas SOD problem, obtained by means of the best implementation of the $AUSM^{+} - up$ scheme adopting the $WENO$ ($5^{th} - 3^{rd}$ order) interpolation, from its initial field towards its final state.

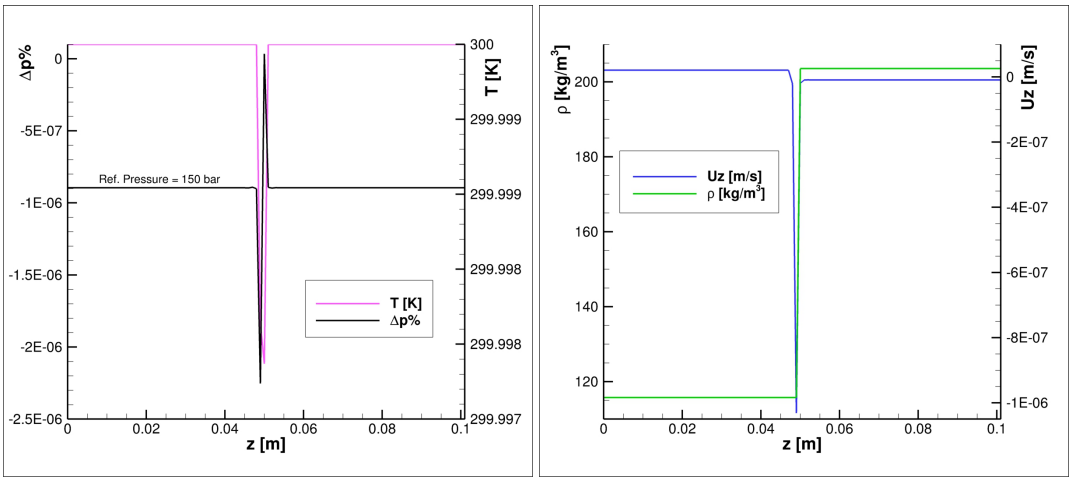

Figura 2.7: Simulation of a real gas still contact discontinuity: percent variation of pressure with respect to the initial 150 bar, temperature, density and velocity profiles after 10000 time steps ($dt = 1.3 \cdot 10^{-7}$ s).

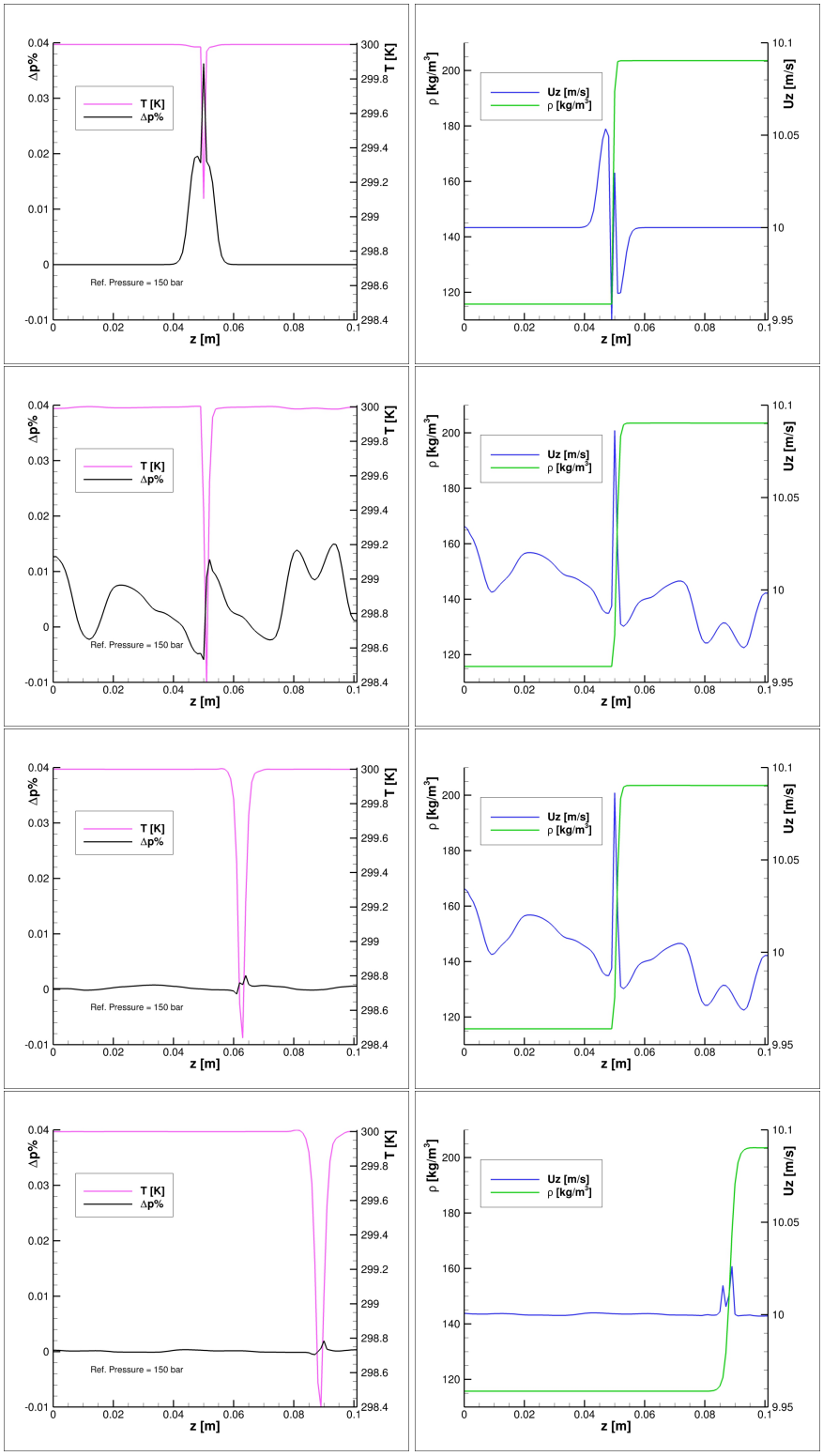

Figura 2.8: Simulation of a real gas moving (10 m/s) contact discontinuity: percent variation of pressure with respect to the initial 150 bar, temperature, density and velocity profiles after 100, 1000, 10000 and 30000 time steps ($dt = 1.3 \cdot 10^{-7}$ s), from top to bottom.

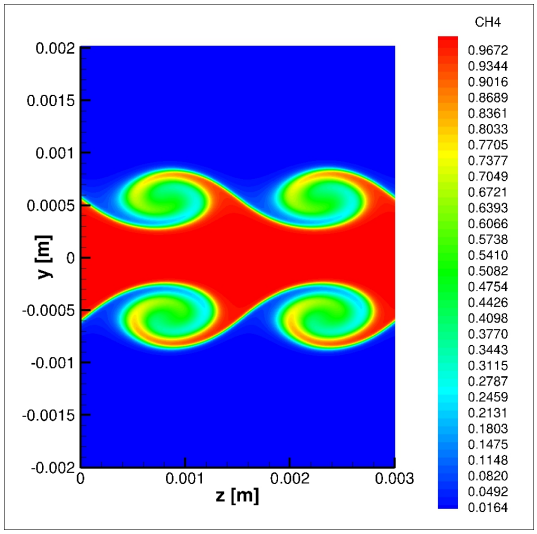

Figura 2.9: Instantaneous CH_4 mass fraction in the ideal gas temporal shear-layer, obtained by means of the best implementation of the $AUSM^+ - up$ scheme adopting the $WENO$ ($5^{th} - 3^{rd}$ order) interpolation.

is simulated with the Peng-Robinson real gas equation of state. The computational domain is two-dimensional with 400 grid nodes uniformly distributed along the streamwise direction and stretched in the crosswise direction. Periodic boundary conditions are assumed in the stream direction, while no-slip adiabatic wall conditions are imposed crosswise. Figure 2.10 shows two instantaneous distributions of N_2 mass fraction: the mixing-layer does not exhibit a laminar roll-up, but there is a quick transition to turbulence. In this simulation the density ranges from nearly $3.5\,kg/m^3$ in the gaseous hydrogen coflow to $560\,kg/m^3$ in the liquid nitrogen central jet. Since this flow is strongly turbulent, the dynamic Smagorinsky subgrid scale model was adopted: the subgrid eddy viscosity, additional to that of the numerical scheme, was found to be critical in reaching a numerically stable solution for this test.

Due to the quick transition to turbulence, it is not possible to compare the temporal evolution obtained by using different numerical schemes. In particular, two solutions were obtained: one with the old version of the $AUSM$ scheme (the one also used in Case 1 of Table 2.1), and the second with the best implementation of the $AUSM^+ - up$ scheme, both adopting the same $WENO$ interpolation. Starting from the same initial already perturbed flowfield, the two solutions are very close for nearly 50000 time-steps ($dt \sim 4.6 \cdot 10^{-10}$ s), but then they rapidly and largely deviate; running the code, the first solution exhibits unphysical temperature undershoots ($\sim 103\,K$, quickly decreasing to $101\,K$) that cause the divergence of the simulation, while the second solution does not (the minimum temperature is $\sim 107\,K$). It is observed that the real gas mixing of nitrogen and hydrogen at the investigated conditions is expected to produce adiabatic mixing temperature lower ($\sim 108\,K$) than the initial temperature of N_2, as shown in Fig. 2.11. An instantaneous snapshot of temperature and density is shown in Fig. 2.12.

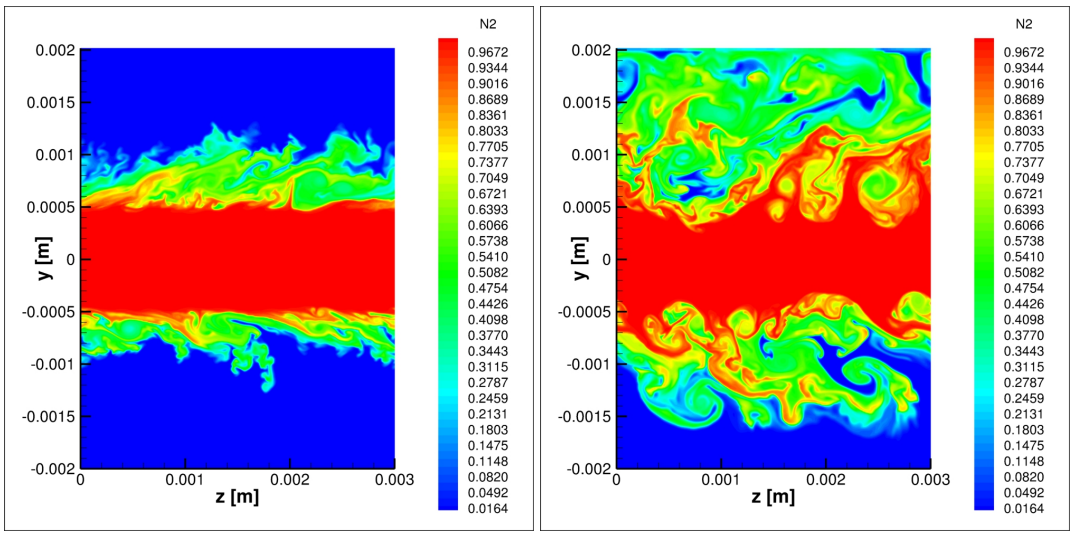

Figura 2.10: Two instantaneous snapshots of the N_2 mass fraction in the real gas temporal shear-layer, obtained by means of the best implementation of the $AUSM^{+} - up$ scheme adopting the $WENO$ ($5^{th} - 3^{rd}$ order) interpolation.

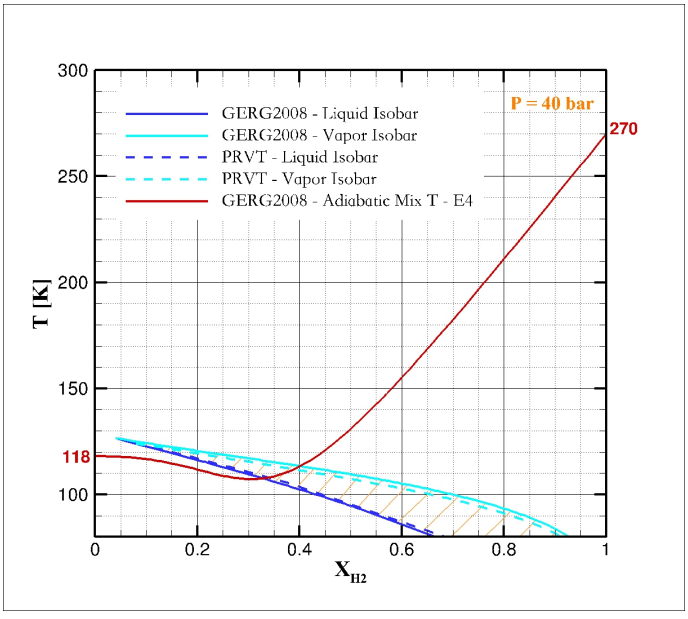

Figura 2.11: Binary phase-diagram for the N_2/H_2 mixture from liquid/vapour equilibrium calculations through REFPROP routines (NIST). The solutions obtained by means of the GERG2008 and the translated-volume Peng-Robinson equations of state are compared.

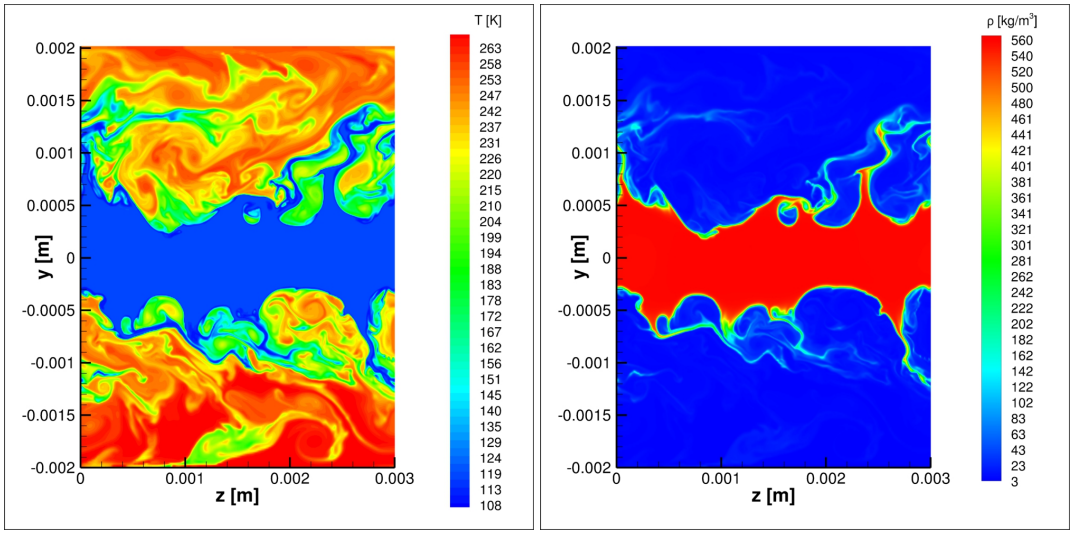

Figura 2.12: Instantaneous snapshot of temperature and density in the real gas temporal shear-layer, obtained by means of the best implementation of the $AUSM^{+} - up$ scheme adopting the $WENO$ ($5^{th} - 3^{rd}$ order) interpolation.

3 Conclusioni

Upon the work done in this year and described in this report, it is concluded that the $AUSM^{+} - up$ numerical scheme, coupled to a robust interpolation procedure ($WENO$ or $QUICK$ in the current implementation in the code HeaRT), can be adopted for numerical simulations of real gas turbulent mixing also dealing with liquid injection that may be found in very-high-pressure gas turbine applications. Thanks also to its real gas extension of the non-reflecting boundary conditions, the ENEA in-house code HeaRT is now an advanced scientific instrument for numerical simulation in parallel computational frameworks.

As an example, a last simulation performed as exploratory study is here reported to introduce the topics that will be investigated in details in the next years: it is the combustion at 295 bar of a central methane jet with a coaxial one of oxygen (strongly diluted in CO_2, 88% in mass), injected in a main stream of CO_2. Such simulation highlights critical problems of flame anchoring due to the high CO_2 concentration, and a not efficient combustion characterized by reacting hot pockets (sometimes reaching very high temperature) dangeroulsy moving towards the turbine downstream of the combustor (see Fig. 3.1). These issues will be investigated by means of the code HeaRT in the next years with the goals of defining a suitable combustion strategy and the injection of reactants, to finally draw a ”concept-design” of the $CH_4/O_2/S - CO_2$ injection plate and of the combustor of a $S - CO_2$ oxy-combustion cycle.

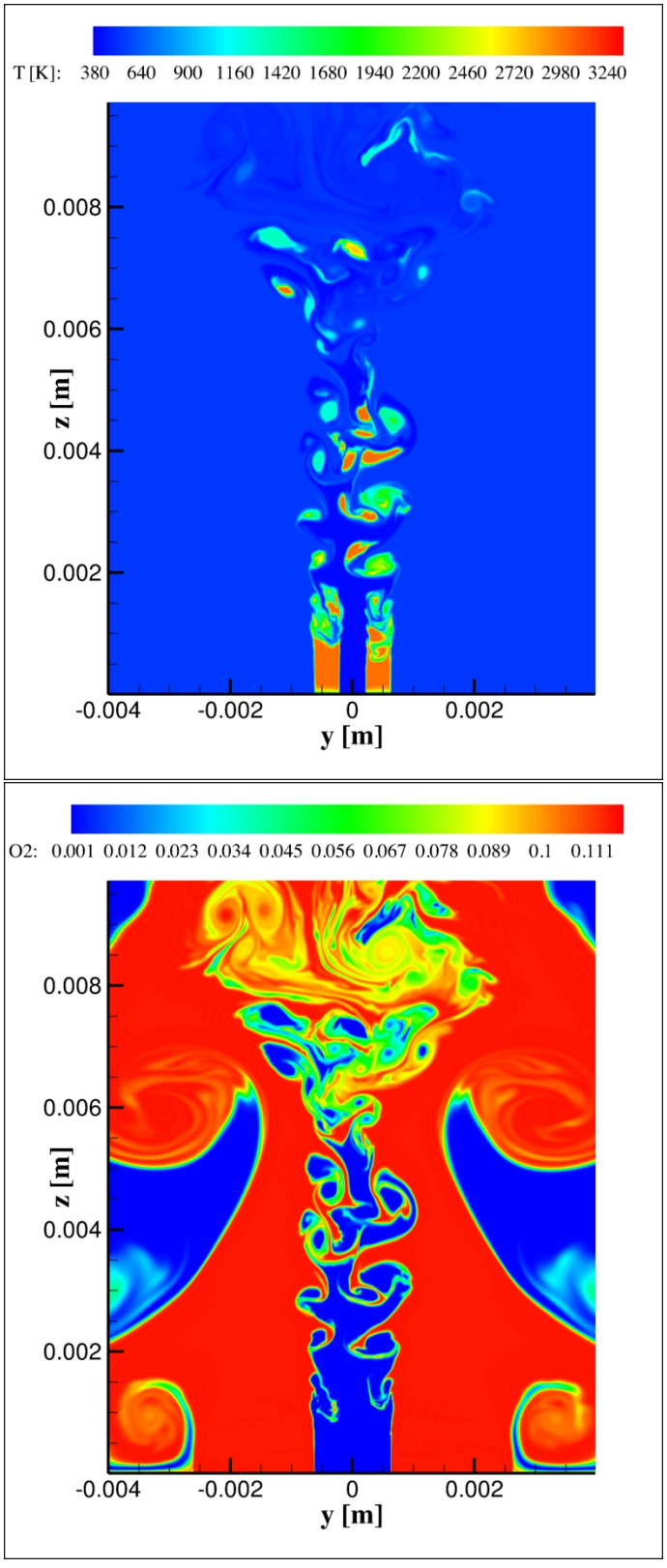

Figura 3.1: Distribuzioni istantanee di temperatura e frazione massica di ossigeno per il test esplorativo reagente metano / ossigeno (fortemente diluito in CO_2) gassosi a 295 bar in condizioni di gas reale.

Bibliografia

[1] David H. Rudy and John C. Strikwerda. A nonreflecting outflow boundary condition for subsonic navier-stokes calculations. *Journal of Computational Physics*, 36(1):55–70, jun 1980.

[2] David H. Rudy and John C. Strikwerda. Boundary conditions for subsonic compressible Navier-Stokes calculations. *Computers & Fluids*, 9(3):327–338, sep 1981.

[3] Kevin W Thompson. Time Dependent Boundary Conditions for Hyperbolic Systems. *J. Comput. Phys.*, 68(1):1–24, jan 1987.

[4] Kevin W Thompson. Time-dependent boundary conditions for hyperbolic systems, II. *Journal of Computational Physics*, 89(2):439–461, aug 1990.

[5] T.J Poinsot and S.K. Lele. Boundary conditions for direct simulations of compressible viscous flows. *Journal of Computational Physics*, 101(1):104–129, jul 1992.

[6] M. Baum, T. Poinsot, and D. Thévenin. Accurate Boundary Conditions for Multicomponent Reactive Flows. *Journal of Computational Physics*, 116(2):247–261, feb 1995.

[7] Guido Lodato, Pascale Domingo, and Luc Vervisch. Three-dimensional boundary conditions for direct and large-eddy simulation of compressible viscous flows. *Journal of Computational Physics*, 227(10):5105–5143, may 2008.

[8] Nora Okong'o and Josette Bellan. Consistent Boundary Conditions for Multicomponent Real Gas Mixtures Based on Characteristic Waves. *Journal of Computational Physics*, 176(2):330–344, mar 2002.

[9] James C. Sutherland and Christopher A. Kennedy. Improved boundary conditions for viscous, reacting, compressible flows. *Journal of Computational Physics*, 191(2):502–524, nov 2003.

[10] E. Giacomazzi, D. Cecere, N. Arcidiacono, and F.R. Picchia. Effetti di condizioni di ingresso di tipo non riflessivo nella simulazione di instabilita' termo-acustiche. PAR2015 RdS/2015/239, ENEA-MiSE, October 2016.

[11] Polifke W. and Wall C. Non-reflecting boundary conditions for acoustic transfer matrix estimation with LES. In *Center for Turbulence Research Proceedings of Summer Program*, Summer 2002. Stanford.

[12] Moguen Y., Bruel P., Perrier V., and Dick E. Non-reflective inlet conditions for the calculation of unsteady turbulent compressible flows at low mach number. In *21st Congres Francais de Mecanique*, 26-30 August 2013.

[13] Axel Coussement, Olivier Gicquel, Benoît Fiorina, Gérard Degrez, and Nasser Darabiha. Multicomponent real gas 3-D-NSCBC for direct numerical simulation of reactive compressible viscous flows. *Journal of Computational Physics*, 245:259–280, jul 2013.

[14] Petit X., Ribert G., and Domingo P. Framework for real-gas compressible reacting flows with tabulated thermochemistry. *The Journal of Supercritical Fluids*, 101:1–16, 2015.

[15] Müller H., Niedermeier M., Jarczyk M., Pfitzner M., Hickel S., and Adams N.A. Large-eddy simulation of trans- and supercritical injection. In *5th European Conference for Aeronautics and Space Sciences (EUCASS)*, July 2013.

[16] X. Petit, G. Ribert, G. Lartigue, and P. Domingo. Large-eddy simulation of supercritical fluid injection. *The Journal of Supercritical Fluids*, 84:61–73, dec 2013.

[17] Hagen Müller, Michael Pfitzner, Jan Matheis, and Stefan Hickel. Large-Eddy Simulation of Coaxial LN2/GH2 Injection at Trans- and Supercritical Conditions. In *53rd AIAA Aerospace Sciences Meeting*, AIAA SciTech. American Institute of Aeronautics and Astronautics, jan 2015.

[18] Schmitt T., Selle L., Ruiz A., and Cuenot B. Large-eddy simulation of supercritical-pressure round jets. *AIAA Journal*, 48(9):2133–2144, September 2010.

[19] Jan Matheis, Hagen Müller, Michael Pfitzner, and Stefan Hickel. Large Eddy Simulation of Cryogenic Coaxial LN2/GH2 Injection under Suparcritical Pressures. In *International Symposium On Turbulence and Shear Flow Phenomena*, Melbourne, Australia, 2015.

[20] Ma P.C., Lv Y., and Ihme M. An entropy-stable hybrid scheme for simulations of transcritical real-fluid flows. *Journal of Computational Physics*, 340:330–357, 2017.

[21] R. Abgrall. How to prevent pressure oscillations in multicomponent flow calculations: a quasi conservative approach. *J. of Computational Physics*, 125(1):150–160, 1996.

[22] H. Terashima and K. Mitsuo. Approach for simulating gas-liquid flows under supercritical pressures using a high order central differencing scheme. *J. of Computational Physics*, 231:6907–6923, 2012.

[23] M.S. Liou, B. van Leer, and J.S. Shuen. Splitting of inviscid fluxes for real gases. *J. of Computational Physics*, 87:1–24, 1990.

[24] M.S. Liou. A new flux splitting scheme. *J. of Computational Physics*, 107:23–39, 1993.

[25] M.S. Liou. The evolution of AUSM schemes. *Defense Science Journal*, 60(6):606–613, 2010.

[26] M.S. Liou. A sequel to AUSM, part II: AUSM$^+$-up for All Speeds. *J. of Computational Physics*, 214:137–170, 2006.

[27] G.A. Sod. A survey of several finite difference methods for systems of nonlinear hyperbolic conservation laws. *J. of Computational Physics*, 27:1–31, 1978.